






## Iceberg Grounding Enhances the Release of Freshwater on the Antarctic Continental Shelf

Anna Olivé Abelló<sup>1</sup> , Pierre Mathiot<sup>1</sup> , Nicolas C. Jourdain<sup>1</sup> , Yavor Kostov<sup>2</sup>,  
Paul R. Holland<sup>2</sup> , Simon Gascoin<sup>3</sup> , and Clement Rousset<sup>4</sup>

<sup>1</sup>Université Grenoble Alpes/CNRS/IRD/INRAE/G-INP, Institut des Géosciences de l'Environnement, Grenoble, France, <sup>2</sup>British Antarctic Survey, Cambridge, UK, <sup>3</sup>Université de Toulouse/CNRS/IRD/INRAE/CNES, Centre d'Etudes Spatiales de la Biosphère, Toulouse, France, <sup>4</sup>LOCEAN-IPSL, CNRS, Sorbonne Université, Paris, France

### Key Points:

- Icebergs inherit the thickness of their calving ice shelf, causing grounding on shallow ridges due to keel depths that often exceed 400 m
- Iceberg grounding increases the amount of meltwater released on the continental shelf by 30%, which increases the ocean stratification
- Iceberg–sea-ice interactions can be parameterized to represent the formation of fast ice and polynyas on either side of grounded icebergs

### Supporting Information:

Supporting Information may be found in the online version of this article.

### Correspondence to:

A. Olivé Abelló,  
[anna.olive-abello@univ-grenoble-alpes.fr](mailto:anna.olive-abello@univ-grenoble-alpes.fr)

### Citation:

Olivé Abelló, A., Mathiot, P., Jourdain, N. C., Kostov, Y., Holland, P. R., Gascoin, S., & Rousset, C. (2025). Iceberg grounding enhances the release of freshwater on the Antarctic continental shelf. *Journal of Geophysical Research: Oceans*, 130, e2025JC022857. <https://doi.org/10.1029/2025JC022857>

Received 14 MAY 2025

Accepted 29 SEP 2025

### Author Contributions:

**Conceptualization:** Anna Olivé Abelló, Pierre Mathiot, Nicolas C. Jourdain, Paul R. Holland  
**Data curation:** Anna Olivé Abelló, Paul R. Holland, Simon Gascoin  
**Formal analysis:** Anna Olivé Abelló  
**Funding acquisition:** Nicolas C. Jourdain  
**Investigation:** Yavor Kostov, Paul R. Holland  
**Methodology:** Anna Olivé Abelló, Pierre Mathiot, Yavor Kostov, Clement Rousset  
**Project administration:** Nicolas C. Jourdain  
**Resources:** Nicolas C. Jourdain, Simon Gascoin

© 2025. The Author(s).

This is an open access article under the terms of the [Creative Commons Attribution License](https://creativecommons.org/licenses/by/4.0/), which permits use, distribution and reproduction in any medium, provided the original work is properly cited.

**Abstract** The importance of Antarctic iceberg meltwater for the Southern Ocean has been a strong incentive to include Lagrangian icebergs in ocean and climate models. However, the modeled iceberg thickness has previously been constrained to 250 m, which appears to be underestimated given the frequent observations of icebergs grounded on substantially deeper bathymetric ridges. In this study, we define the initial iceberg thickness based on the thickness of the ice shelf from which they calve and rationalize the way to define the iceberg size classes. Ocean–sea-ice–iceberg simulations reveal that more than half of the iceberg melting is discharged over the Antarctic continental shelf, reaching an average of 631 Gt yr<sup>−1</sup> when the interaction of icebergs with bathymetry is neglected, and 802 Gt yr<sup>−1</sup> when a simple grounding scheme is implemented. Such additional freshwater injected over the continental shelf prone to sea ice production has important consequences for the ocean properties around Antarctica. It enhances ocean stratification, inhibits deep convection and isolates dense deep waters from the colder and fresher surface layers. This isolation allows the deep waters to warm and become saltier, thereby intensifying subsequent ice-shelf melting. Moreover, the simulated distribution of grounded icebergs blocks drifting sea ice, promoting the formation of thick sea ice and polynyas when the fast ice parameterization is included. This work emphasizes the need for further research into the physical representation of iceberg grounding and iceberg–sea-ice interaction.

**Plain Language Summary** Antarctic icebergs are very important for the Southern Ocean's water cycle because they release substantial amounts of freshwater when they melt. Despite their crucial role, some climate models do not accurately represent how thick these icebergs (often seen grounded in deep waters) can be, causing freshwater to be unrealistically distributed along their drift paths instead of at grounding sites. In this study, we improve one of these models by considering the thickness of the ice shelf from which they broke off and defining the iceberg sizes in a way that better represents their actual distribution. Our simulations show that over half of the melting from Antarctic icebergs occurs over shallow areas near and around the continent. When we include a simple approach for thick icebergs to get stuck on submarine ridges in the model, the amount of freshwater released into shallow areas around the continent increases significantly. This extra freshwater changes the ocean properties around Antarctica, making the water layers more stable, which can limit the mixing of deep and surface waters. Finally, stuck thick icebergs can block the drifting sea ice when simple iceberg–sea-ice interactions are simulated, causing thicker ice on one side and open water on the other.

## 1. Introduction

Meltwater released from Antarctic icebergs is quantitatively comparable to the Antarctic ice-shelf basal melt (Davison et al., 2023), thus constituting a substantial component of the Southern Ocean freshwater cycle. However, their melting patterns differ significantly. While the ice shelf meltwater is released in front of the Antarctic continent, icebergs can travel long distances and melt all over the Southern Ocean (e.g., Tournadre et al., 2015; Wagner et al., 2017). Their melting may locally alter the ocean salinity and temperature within the upper several hundred meters of the water column. Near the icebergs, surface meltwater freshens the ocean surface, forming a shallow, low-salinity layer that promotes sea ice formation, enhances surface stratification, and suppresses ocean convection (Ackermann et al., 2024; Jongma et al., 2009; Merino et al., 2016). Depending on the relative iceberg–ocean velocity and on the iceberg size, basal meltwater released at depth may disrupt the stratified structure of the Winter Water (WW) layer and induce vertical mixing of nutrient-rich, warm, and saline Circumpolar Deep Water (CDW) with the surface layer (FitzMaurice et al., 2017; Lucas et al., 2025). Such

**Software:** Anna Olivé Abelló,  
Pierre Mathiot, Clement Rousset  
**Supervision:** Pierre Mathiot, Nicolas  
C. Jourdain  
**Validation:** Anna Olivé Abelló, Nicolas  
C. Jourdain  
**Writing – original draft:** Anna Olivé  
Abelló  
**Writing – review & editing:**  
Pierre Mathiot, Nicolas C. Jourdain,  
Yavor Kostov, Paul R. Holland,  
Simon Gascoin, Clement Rousset

freshwater-driven changes in the upper-ocean characteristics and structure may have far-reaching implications in the Earth's climate system. Indeed, some model projections suggest that a future increase in iceberg melt could delay atmospheric warming in the Southern Hemisphere and activate a positive feedback between surface freshening, subsurface warming and ice-sheet/shelf melting, which could accelerate ice mass loss around Antarctica (Schloesser et al., 2019).

Despite their importance in the freshwater flux distribution, a large number of climate models do not make any distinction between ice-shelf and iceberg melt (e.g., Voldoire et al., 2019). Some distinguish icebergs but prescribe iceberg melt either uniformly over a predefined region (e.g., Devilliers et al., 2021) or following a spatial pattern from other modeling studies (e.g., Boucher et al., 2020). Iceberg trajectories and melting have started to be explicitly represented in some models (Ackermann et al., 2024; Jongma et al., 2009; Schloesser et al., 2019; Smith et al., 2021; Stern et al., 2016; Thomas et al., 2023), but this remains relatively rare, especially in global climate models contributing to the Coupled Model Intercomparison Project (CMIP). These studies represent individual icebergs or groups of icebergs as Lagrangian particles, and the imposed calving flux, from satellite products or ice sheet models, is distributed into several iceberg classes of predefined size and thickness (Bigg et al., 1997; Martin & Adcroft, 2010).

Most modeling studies have used a thickness of 250 m for the largest iceberg classes (Marsh et al., 2015; Martin & Adcroft, 2010; Merino et al., 2016; Rackow et al., 2017; Stern et al., 2015), following the typical ice-shelf thickness suggested by Gladstone et al. (2001) independently of the calving location. However, ice-shelf thickness at the calving front varies considerably, ranging from less than 50 m to as much as 680 m (Dowdeswell & Bamber, 2007; Morlighem et al., 2020). The ice thickness varies between ice shelves and along the front of a given ice shelf. For instance, it lies within  $150 \pm 50$  m along the eastern front of Ronne Ice Shelf, within  $350 \pm 100$  m along the Ross Ice Shelf front, and  $500 \pm 250$  m along the Filchner Ice Shelf front (Morlighem et al., 2020; Rignot et al., 2013; Scambos et al., 2007). Furthermore, icebergs have been observed to ground at depths of up to 400 m in East Antarctica and in the Amundsen Sea, and scours on the continental shelf suggest that these could even reach 500 m (Beaman & Harris, 2005; Massom, 2003; Massom et al., 2009; Mazur et al., 2017). Measurements of the freeboard of large tabular icebergs through satellite radar and laser altimetry confirm the existence of icebergs thicker than 400 m (Scambos et al., 2005; Tournadre et al., 2015). Hence, the aforementioned ocean modeling studies have clearly underestimated the upper end of the iceberg thickness distribution.

Being unable to reproduce accurately the iceberg thickness in ocean models may prevent icebergs from grounding on shallow bathymetric ridges. This has significant implications, as grounded icebergs act as anchor points for sea ice, promoting the formation of thicker sea ice that remains fastened to them (Fraser et al., 2021; Massom & Stammerjohn, 2010; Remy et al., 2008). For instance, the semi-permanent grounded iceberg region and associated fast ice over Bear Ridge (Figure 1) has not been well-represented in ocean models and must be precisely outlined to ensure accurate representation of the ocean properties on the Amundsen Sea continental shelf (Bett et al., 2020; Nakayama et al., 2014). Such fast ice favors the opening of coastal polynyas, as the Amundsen Sea Polynya, where most of the Antarctic sea ice is produced (Hou & Shi, 2021; Huot et al., 2021; Massom et al., 2001; Van Achter, Fichet, Goosse, Pelletier, et al., 2022). Simulating their presence and grounding zones properly in ocean models would improve our ability to project future sea-ice production rates and water mass transformation, including Antarctic Bottom Water formation (Fraser et al., 2021; Kusahara et al., 2017; Massom et al., 2001; Ohshima et al., 2013; Van Achter, Fichet, Goosse, & Moreno-Chamarro, 2022).

In this paper, we propose a novel approach in which the maximum iceberg thickness depends on the ice-shelf thickness at the calving location. We implement these changes as well as a simple grounding scheme in a circum-Antarctic ocean–sea-ice model (Section 2). Then, we analyze the impacts of the melting distribution on the sea-ice thickness and ocean bottom temperature and salinity (Section 3). Finally, we discuss the consistency of our results with observational estimates of Antarctic fast ice, evaluate the ability to reproduce fast ice and polynyas through two different simple approaches, and propose future possible improvements to the model (Section 4).

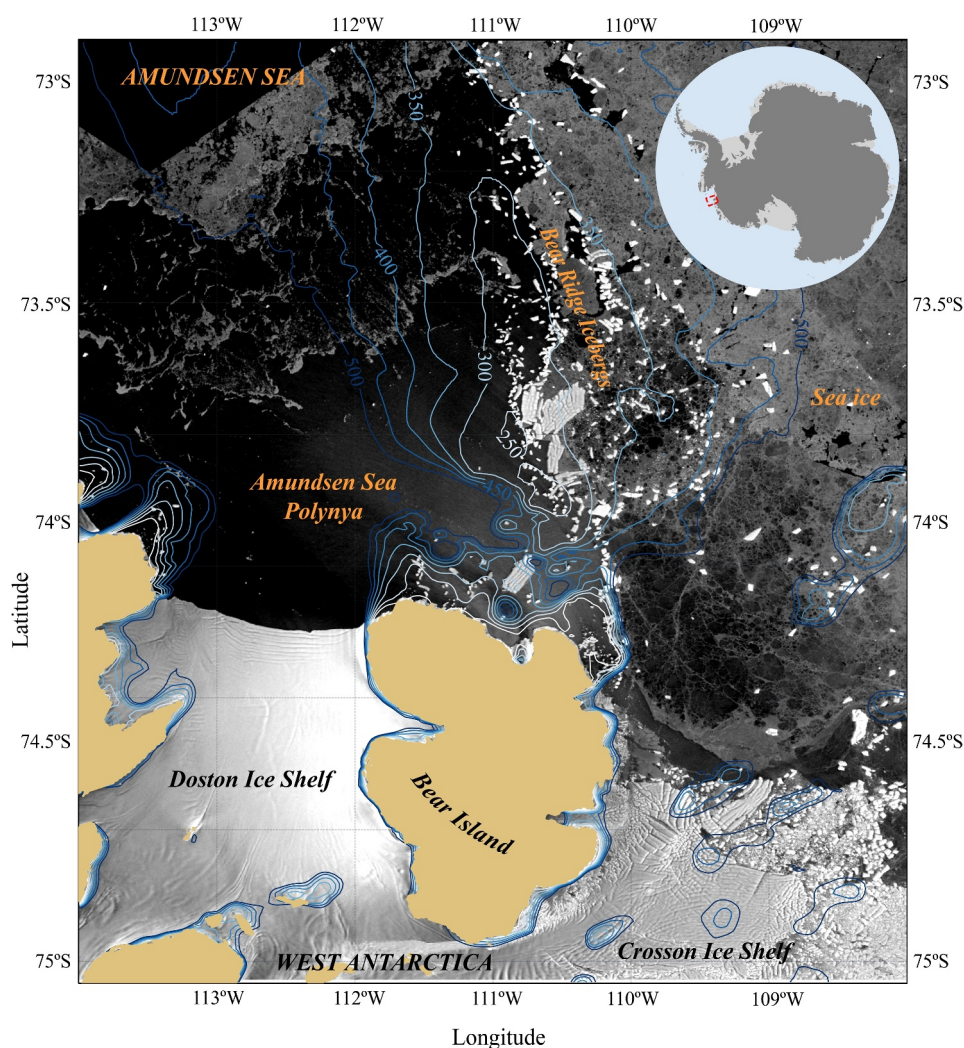


**Figure 1.** Sentinel-1 Synthetic Aperture Radar satellite image taken on 2023-11-24 of the semi-permanent feature called Bear Ridge Icebergs (BRI), in the Amundsen Sea, with the IBCSO isobath contours (in blue) that range from 250 to 500 m (Arndt et al., 2013). The satellite image has been obtained through the Interferometric Wide Swath technique and in Ground Range Detected format. The land-based ice mask, from the Antarctic Digital Database and based on grounding line data included in BedMachine-v3 (Morlighem, 2022), is represented in sandy brown. Note the sea ice trapped to the east of the BRI, and open the Amundsen Sea Polynya to the west.

## 2. Models and Methods

### 2.1. The Ocean–Sea-Ice Model Configuration

We use the Nucleus for European Modeling of the Ocean (NEMO), version 4.2.0, to represent the ocean dynamics and physics (NEMO-OPA, Madec & the NEMO System Team, 2022) together with the sea ice dynamics and thermodynamics (SI<sup>3</sup>, NEMO Sea Ice Working Group, 2019). The model simulates the ocean circulation and interactive melting under ice shelves (Mathiot et al., 2017), as well as the motion and melting of icebergs (see following Subsection).

The circum-Antarctic configuration used, referred to as eANT025.L121, is an extraction of the global configuration described in Mathiot and Jourdain (2023), with a northern domain boundary at 52.25°S. The horizontal resolution is  $0.25^\circ \times 0.25^\circ \cos(\text{lat})$  in latitude  $\times$  longitude, with 121 vertical levels enabling a vertical resolution of  $\sim 20$  m at typical ice-shelf base depths (between 100 and 1,000 m depth). The model setup is the same as in Mathiot and Jourdain (2023), except that we do not apply the freshwater flux correction that is needed to avoid the global model drift.

Our simulations are forced by a repeated year of 3-hourly atmospheric forcing from the Japanese 55-year Reanalysis (JRA55-do) (Kobayashi et al., 2015; Tsujino et al., 2018) through the CORE bulk formulae described in Griffies et al. (2009) and Large and Yeager (2004). The repeated cycle spans from 01 May 1990 to 30 April 1991, which was identified as the optimal normal-year data set for driving ocean–sea-ice models by Stewart et al. (2020). Using a repeated year, we can more easily identify when a steady state is reached, enabling a clearer comparison between experiments. The northern ocean boundary conditions are derived from 5-day mean outputs of Mathiot and Jourdain (2023) and are applied over the same repeated period.

## 2.2. The NEMO Iceberg Module

The iceberg module in NEMO treats icebergs as Lagrangian particles, each particle being representative of one iceberg or a group of multiple icebergs with identical characteristics (Marsh et al., 2015).

### 2.2.1. Icebergs Dynamics and Thermodynamics

The iceberg dynamics are governed by the Coriolis force, air and ocean drag, horizontal ocean pressure gradients, wave radiation forces, and sea-ice drag (Martin & Adcroft, 2010). Moreover, the vertical structure of ocean currents is accounted for in the ocean drag calculation (Merino et al., 2016). In our model, icebergs do not influence the ocean or the sea-ice momentum equations, a limitation that is discussed in Section 4. Given that our configuration has an open boundary at 52.25°S, we have also modified NEMO so that any iceberg reaching the northern boundary is immediately removed from the system, which is only relevant for the Weddell Sea sector (longitudinal boundaries defined in Section 3.2). Hence, icebergs cannot re-enter the model domain.

In this study, we use a very simple approach to represent the iceberg interaction with bathymetry, which we hereafter refer to as the grounding scheme, although it does not explicitly resolve the grounding and ungrounding processes. If the iceberg keel is deeper than bathymetry at a given time step, it is immediately sent back to its previous position and its horizontal velocity is set to zero. It implies that the iceberg then remains at this previous position until the action of the ocean and/or winds set it in motion again.

The mass balance of each iceberg is determined by basal melting, convective melting along its sidewalls and wave erosion (Bigg et al., 1997). The freshwater and latent heat fluxes related to these three terms are calculated at each time step and injected at the ocean surface. The vertical structure of ocean temperatures and salinity is accounted for in the melt rate calculation (Merino et al., 2016).

### 2.2.2. Icebergs Calving

The iceberg module receives as input the calving flux of Rignot et al. (2013), which assumes a steady-state calving front as in our simulations. Given that observational calving fluxes are only available for entire ice shelves, we randomly distribute the calving flux across the ocean grid points along a given ice shelf front. The calving flux at a given location is then distributed into  $N$  iceberg classes, each of which represents a particular surface area, following the observed distribution of the number of icebergs in the Southern Ocean per iceberg surface area (Åström et al., 2021; Tournadre et al., 2016). For each class at a given location, an iceberg particle is calved when the distributed calving flux has put enough mass to form a particle with the surface area and thickness of that class. To save spin-up time, each iceberg class at each calving location starts partly filled in a random way. To do so, the total ice mass required to release one particle for each iceberg class was multiplied by a random seed value, between 0 and 1, ensuring reproducibility between experiments (all simulations are described in detail in Section 2.3).

To estimate lateral melt rates and drag, we need to make some assumptions about the horizontal length and width of icebergs for a given surface area class. To find the most reliable length/width ( $\ell/w$ ) ratio for the Antarctic tabular icebergs, the dimensions of 150 random icebergs were manually estimated from Sentinel-1 C-band Synthetic Aperture Radar (SAR) backscatter images (European Space Agency, 2019) of the Amundsen Sea in 2014–2015 at a horizontal resolution of 50 m (Figure S1 in Supporting Information S1). For that, we extracted a time series of single co-polarization (horizontal transmit/receive) images from ascending orbits in extra wide and interferometric wide swath modes, from the Ground Range Detected collection in Google Earth Engine (Gorelick et al., 2017), enhancing sensitivity to ocean–iceberg–sea-ice features and consistent illumination geometry

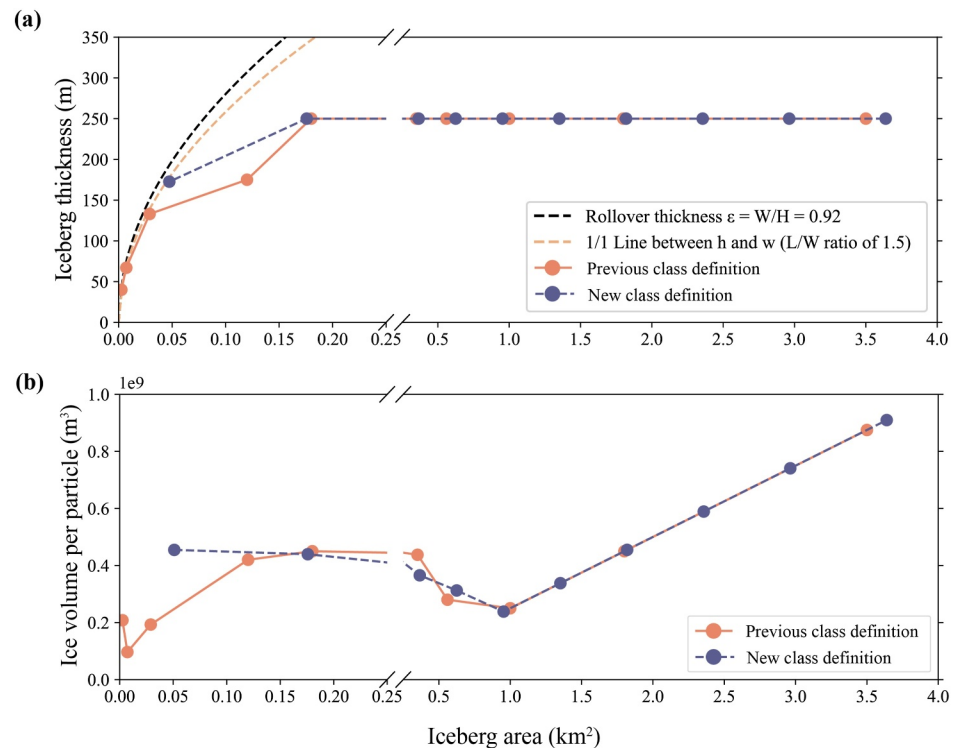


**Figure 2.** (a) Thickness of calved icebergs and (b) ice volume of particles using the new class and thickness definition for 10 iceberg classes (in purple dashed line) and compared to the previous class definition by Stern et al. (2016) (in orange solid line). The newly estimated iceberg thickness per class has been computed considering a local ice-shelf thickness of 250 m (see Appendix A1 for further clarification on the definition of the iceberg classes), for better comparison with the previous class definition. Note that the ice volume does not increase monotonically with iceberg area for the smaller classes, since it is computed as  $V_k = n_k \langle h \rangle_k \langle a \rangle_k$ , where  $n_k = 52, 10, 5, 3, 2, 1, 1, 1, 1$  and 1 for a clustering parameter  $R = 2$ .

(Dierking, 2013). We found a median  $\ell/w$  of  $1.42 \pm 0.80$ , and therefore adopt the commonly used coefficient  $\ell = 1.5w$  from previous studies (e.g., Bigg et al., 1997; Silva et al., 2006; Stern et al., 2016).

In previous work, the iceberg thickness of individual classes was set to empirical values independently from the calving location, with a maximum of 250 m thickness for the largest icebergs. In our new approach, all icebergs are calved with a thickness  $h$  corresponding to the ice-shelf thickness at the closest calving front, which is estimated from the BedMachine-v3 data set (Morlighem, 2022; Morlighem et al., 2020). For the classes in which the iceberg width is smaller than the ice-shelf thickness, the thickness of the calved iceberg is reset to the width value (Figure 2a). Exceptionally, the bathymetry on the NEMO grid can be shallower than the ice-shelf draft from BedMachine-v2 in calving grid cells. In this case, the iceberg thickness is capped at 99% of the local water depth to prevent the iceberg accumulation. During the simulation, a melting iceberg rolls over when  $w/h < 0.92$ , a threshold calculated from the expression of MacAyeal et al. (2003) using our model density values (Bonnet et al., 2020).

### 2.2.3. Definition of the Iceberg Classes

In previous studies, the NEMO iceberg module was used with 10 classes of empirical characteristics: from 60 to 2,200 m in horizontal length, and an ice-shelf thickness of 250 m for the largest classes. In Merino et al. (2016), the surface area of individual icebergs in a 10-class distribution was defined as  $a = w\ell = 0.003, 0.007, 0.029, 0.12, 0.18, 0.35, 0.56, 1.0, 1.8$ , and  $3.5 \text{ km}^2$ . Here, we propose a new approach to objectively define the horizontal iceberg size for any number of classes  $N$ , in a way that each of the classes represents a similar ice volume. A similar ice volume implies that iceberg calving will occur more frequently for the smaller classes. Clustering multiple icebergs into a single Lagrangian particle allows for avoiding simulating an excessive number of particles that contribute negligibly to the freshwater budget, while also providing greater flexibility in the choice of the number of classes.

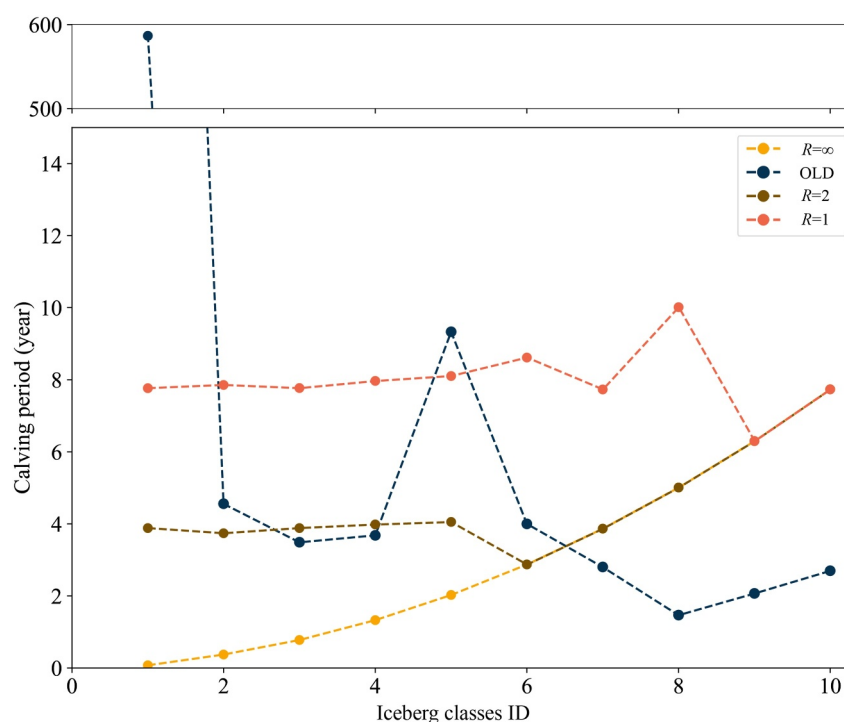


**Figure 3.** Period required to release one Lagrangian particle per class, assuming a calving rate of  $1 \text{ Gt yr}^{-1}$ . OLD experiment corresponds to the classical class definition of Stern et al. (2016) and different values of the clustering parameter,  $R$ , have been applied to the new class definition.

Moreover, as each iceberg class receives approximately the same ice volume per year, the calving of small icebergs will also be more frequent. Although this is realistic (e.g., Fricker et al., 2002; MacKie et al., 2024)—as giant icebergs are formed in large and infrequent calving events, smaller icebergs are formed by frequent processes, such as the extension of the ice due to gradients in boundary friction, tensile and shear stresses at ice fronts, undercutting by subaqueous melting, and torque from buoyant forces (Benn & Åström, 2018)—the high computational cost of tracking many small icebergs, which only contribute a small freshwater flux, motivates the clustering of multiple icebergs into a single Lagrangian particle. To keep a reasonable representation of the spatial dispersion of small icebergs while limiting the computational cost, we define a clustering parameter,  $R$ , in a way that an iceberg class is not able to produce a Lagrangian particle more than  $R$  times more often than the largest class (Figure 2b). All particles thus represent a similar ice volume when  $R \rightarrow 1$ , while there is no clustering when  $R \rightarrow \infty$ .

To find the most suitable  $R$  value, we estimate the calving period after which the Lagrangian particles are released for a typical calving flux of  $1 \text{ Gt yr}^{-1}$  (Figure 3). With  $R = 1$  (maximum clustering), the class with the smallest icebergs releases a Lagrangian particle every 8 years, a period that is reduced by half for  $R = 2$ . Instead, when  $R$  is very large (no clustering), this class releases a particle every 27 days. In this case, the total number of particles can increase substantially, and the computational cost increases significantly (see Appendix A2). In comparison, the class definition and clustering of Stern et al. (2016), used in our OLD experiment, gives a particle release every 589 years for the smallest icebergs (Figure 3). With 10 classes, we have found that  $R = 2$  gives a similar total number of particles as in classical distributions (Figure S2 in Supporting Information S1), and we use this value throughout the manuscript for a meaningful comparison with the classical distributions. The sensitivity to the  $R$  parameter is investigated in Appendix A2.

While the total heat and freshwater flux contributions are multiplied by the number of icebergs in the clustered particle, the calculations for the average iceberg characteristics are done for a single iceberg. The approach used to estimate average iceberg characteristics ( $\langle a \rangle_k, \langle h \rangle_k$ ) in each class  $k$  is detailed in Appendix A1. In short, we assume that the iceberg size distribution during calving is the same as the one observed in the Southern Ocean, with a probability of iceberg occurrence following  $a^{-1.5}$  as a good approximation (Åström et al., 2021; Tournadre

**Table 1**

Example of Iceberg Characteristics Across Individual Size Classes, Considering 10 Classes, a Clustering Parameter Corresponding to  $R = 2$ , and an Ice-Shelf Thickness of 250 m at the Calving Front

Size class	Initial iceberg mass (kg)	Initial iceberg area (km <sup>2</sup> )	Initial iceberg length (m)	Initial iceberg thickness (m)	Number of icebergs in a particle	Calving mass flux distribution
1	$7.47 \cdot 10^9$	0.05	276	173	52	0.1
2	$3.74 \cdot 10^{10}$	0.18	514	250	10	0.1
3	$7.77 \cdot 10^{10}$	0.37	740	250	5	0.1
4	$1.33 \cdot 10^{11}$	0.62	968	250	3	0.1
5	$2.03 \cdot 10^{11}$	0.95	1,196	250	2	0.1
6	$2.87 \cdot 10^{11}$	1.35	1,424	250	1	0.1
7	$3.87 \cdot 10^{11}$	1.82	1,652	250	1	0.1
8	$5.01 \cdot 10^{11}$	2.36	1,880	250	1	0.1
9	$6.30 \cdot 10^{11}$	2.96	2108	250	1	0.1
10	$7.73 \cdot 10^{11}$	3.64	2336	250	1	0.1

*Note.* The total particle mass per size class can be calculated by multiplying the number of icebergs represented in one Lagrangian particle by the initial iceberg mass.

et al., 2016). After 40 years of simulation (described in detail in Section 2.3), the resulting iceberg size distributions within the domain broadly support this assumption, with the observed underrepresentation of the smallest icebergs likely due to both the absence of calving particles smaller than 0.05 km<sup>2</sup> and the lack of fragmentation processes (see Figure S3 in Supporting Information S1). Moreover, as we do not represent the fragmentation of icebergs during their trajectories, we impose an upper bound to the size distribution, which we set to  $a_{\max} = 4$  km<sup>2</sup>. Keeping larger icebergs would produce trajectories that extend unrealistically far north (England et al., 2020; Rackow et al., 2017). For the sake of simplicity, computational cost and uniformity of treatment around Antarctica, we use the same  $\langle a \rangle_k$  values, that is, the same class definition, at all calving points. For the 10-iceberg class distribution, the corresponding surface areas per class are  $\langle a \rangle_k = 0.05, 0.18, 0.37, 0.62, 0.95, 1.35, 1.82, 2.36, 2.96$ , and 3.64 km<sup>2</sup> (Table 1). Table 1 shows all iceberg characteristics per class calculated in a way that ensures an equal distribution of the calving mass flux into  $N$  classes for a typical ice-shelf thickness of 222.5 m (see the justification of this value in Appendix A1, especially in Figure S4 in Supporting Information S1). For local ice shelf thicknesses, the actual mass distribution is therefore not perfectly even, but this is still better distributed than with previous empirical choices.

### 2.3. Experiments

Four experiments are run for 40 years with an initial state completely free of icebergs (Table 2). All of them consider 10 iceberg classes. The OLD experiment adopts the classical thickness and size distribution from Stern et al. (2016), prescribes a maximum iceberg thickness of 250 m, and does not represent iceberg grounding. The NoGr250 is similar to OLD, considering also a maximum constant of 250 m thickness for the ice shelves, but implementing our objective definition of iceberg classes (with  $R = 2$ ). The NoGr is the same as NoGr250, apart from the use of the actual Antarctic ice shelf thickness to determine the iceberg thicknesses and the REF

**Table 2**

Description of the NEMO Experiments Used in This Study

Experiment name	Classes definition	Number of classes	Ice-shelf thickness	Grounding scheme	$R$ param. (clustering)
OLD	Classical	10	250 m	None	–
NoGr250	New	10	250 m	None	2
NoGr	New	10	BM	None	2
REF	New	10	BM	$u = 0, v = 0$	2

*Note.* BM stands for BedMachine,  $u$  and  $v$  represent the zonal and meridional components of horizontal velocity and the sensitivity to these choices is analyzed in Appendix A2.

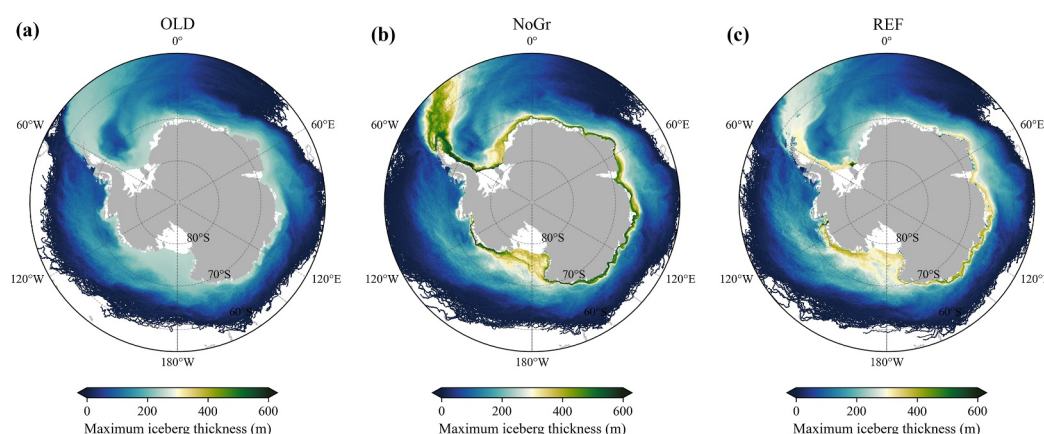


**Figure 4.** Maximum iceberg thickness per grid cell in the 25-year climatology for (a) the OLD experiment with a maximum iceberg thickness of 250 m, (b) the NoGr experiment with the iceberg thickness determined by the Antarctic ice-shelf thickness at the calving front, both in the absence of a grounding scheme, and (c) the REF experiment that is similar to NoGr but includes a grounding scheme.

experiment is the same as NoGr, apart from the inclusion of the iceberg grounding scheme. Additionally, two sensitivity studies are conducted to assess how the clustering parameter  $R$  and the number of iceberg classes  $N$  influence the resulting freshwater flux distribution (see Appendix A2), and two extra short-term experiments to evaluate the iceberg module's ability to simulate the impact of grounded icebergs on sea ice dynamics described in Section 4.

### 3. Results

#### 3.1. Iceberg Maximum Thickness and Grounding Occurrence

The spin-up period is estimated to last approximately 15 years, after which the total mass of icebergs in the Southern Ocean reaches a steady state— except in the REF experiment, where the ice volume continues accumulating, reaching twice that of the other experiments (see Appendix A3 for further details). We then calculate the steady-state climatology by averaging the following 25 years.

To visualize the characteristics of icebergs in the Southern Ocean, we define the iceberg maximum thickness in a model grid cell as the highest thickness among all icebergs crossing that cell. The 25-year climatology of the iceberg maximum thickness distribution across the Southern Ocean varies notably depending on whether the actual ice-shelf thicknesses are considered (Figure 4). In contrast to the previous scheme (OLD experiment; Figure 4a), which did not allow icebergs to be thicker than 250 m, accounting for the Antarctic ice-shelf thickness at the calving front (NoGr experiment; Figure 4b) produces icebergs of up to 680 m thick. Such thick icebergs, driven mostly by ocean drag and Coriolis force along the Antarctic coast, are mostly found over the Antarctic continental shelf, carried by the counterclockwise Antarctic Coastal Current (ACoC), and leaving the domain northward through the well-known *Iceberg Alley* in the western Weddell Sea. Thus, incorporating local Antarctic ice-shelf thicknesses into the new formulation for iceberg thickness distribution leads to a wider range of thicknesses and a broader dispersion of icebergs, especially for the smaller ones reaching lower latitudes in the Pacific sector, easily moved northwards by katabatic winds and quickly entrained by the Antarctic Circumpolar Current (ACC; Figure 4b).

The iceberg maximum thickness pattern changes completely when grounding is activated. While thick icebergs are found all along the Antarctic coast in the absence of grounding scheme (NoGr), implementing both a realistic thickness and a grounding scheme prevents them from crossing submarine ridges shallower than their keel depth. As observed in Figure 4c, icebergs become grounded along the Antarctic continental shelf generally near their calving points, where they may remain until either melting reduces their thickness enough to cross the bathymetric obstacle or external forces dislodge them (e.g., wind direction, sea surface height, ocean pressure gradients). This results in many of the thickest icebergs being trapped in front of various ice shelves, particularly the Thwaites Glacier and Ronne-Filchner Ice Shelf, and then leaving their respective regions with significantly

smaller thickness than they had after calving. This extends the residence time of the thickest icebergs in the Southern Ocean, especially over the continental shelf where shallow ridges are found and where upper-ocean water temperatures remain cold.

The probability of an iceberg grounding in open ocean waters, away from the Antarctic continental shelf, is negligible unless islands or submarine ridges are present. Based on the grounded iceberg distribution in REF, the most likely grounding zone on the Antarctic continental shelf comprises mainly bathymetry from 0 to 400 m (91% of the grounded iceberg grid cells), especially in front of the thickest ice shelves such as the Ross Ice Shelf (Ross, Pennell and Mawson Banks), Ronne-Filchner Ice Shelf (Bjerkner Bank) and Thwaites Glacier (Bear Ridge) (Figure S5 in Supporting Information S1). These shallow banks not only trap thick icebergs calving directly from the closest ice shelves, but also those drifting westward from other regions. A few regions stand out as having one iceberg grounded per grid cell more than 75% of the time: the Black Coast on the eastern side of the Antarctic Peninsula, the coast of Victoria Land in the western Ross Sea and in several places along the East Antarctic coast (see Figure S5b in Supporting Information S1 for the location of these regions).

In the Amundsen Sea, the grounded iceberg frequency in our reference simulation (REF) fairly reproduces the distribution of iceberg occurrence observed from Sentinel-1 SAR satellite images in 2011 (Figure 5). The distribution of iceberg occurrence product provided by Mazur et al. (2017) is based on an algorithm for automatic iceberg detection applied to 432 radar satellite images, effectively identifying the smaller icebergs. In Figure 5, the high probability of iceberg presence is centered on the eastern side of ridges, indicating a westward drift of the bergs. The frequency of grounded icebergs in our simulation is notably higher near the coast, where bathymetry is shallower. While the REF experiment only shows maximum frequencies, that is permanent iceberg presence, close to the Amundsen Sea coast, observations reveal that icebergs indeed remain grounded nearly the entire year along the whole extent of the submarine ridges. The tendency to generally underestimate iceberg permanence in the REF simulation relative to observational data is examined in greater detail in Section 4.

### 3.2. Effect of Iceberg Grounding on the Freshwater Fluxes

Once the Antarctic tabular icebergs are calved, they melt progressively along their trajectory over the Southern Ocean. Since some icebergs (about 3%–5%) exit the domain north of 52.25°S without melting completely, the total iceberg melt estimated and accumulated in the region in the experiments does not perfectly balance the calving rate of 1,265 Gt yr<sup>−1</sup>. Indeed, icebergs leaving the domain contribute with an average imbalance of  $50 \pm 11$  Gt yr<sup>−1</sup> for the OLD, NoGr, and REF experiments. Most of the mass exported outside the domain corresponds to small, thin bergs, with 86% of the grid cells along the domain boundary exhibiting maximum thicknesses below 25 m (Figure 4c).

The 25-year climatological mean of iceberg melting inside the domain for these experiments corresponds to  $1187 \pm 5$  Gt yr<sup>−1</sup> and the total mass of icebergs still present in the domain (i.e., not yet melted) varies on average from 3,030 Gt without grounding (NoGr) to 5,360 Gt with grounding (REF; see Appendix A3 for further discussion). Thanks to our new approach for defining iceberg size classes and clustering, the ice-shelf discharge flux stored until a particle of a given size class is filled and ready to calve is rapidly replaced in the NoGr and REF experiments. In contrast, the OLD experiment still accumulates about 7 Gt yr<sup>−1</sup> of mass that has not yet calved, as many particles remain unreleased even after 25 years of simulation (see Figure 3 and Section 2.2).

Our iceberg melt pattern shows the highest values along the Antarctic continental shelf and in the northwestern Weddell Sea, specially through the Iceberg Alley (Figure 6a). This melting pattern is more diffuse than the model climatology of Merino et al. (2016) because their iceberg size distribution was biased toward small icebergs. Martin and Adcroft (2010) and other authors indeed wrongly interpreted the calving-size distribution as a calving mass flux distribution, as discussed in Stern et al. (2016). The activation of the grounding scheme modifies this melt pattern (Figure 6b). Considering six large Antarctic sectors, the Weddell Sea is the only one where the sector-averaged melt flux decreases significantly when icebergs ground, from 637 to 442 Gt yr<sup>−1</sup>, receiving significantly less freshwater, especially over the north of the Antarctic Peninsula and Riiser-Larsen Basin (Figure 6b). In contrast, all other sectors exhibit higher melt rates when icebergs ground, with the smallest increase in the Bellingshausen Sea, in agreement with Merino et al. (2016). This is likely due to the fact that the Bellingshausen Sea is not supplied by icebergs from upstream sources along the ACOC. Given Figures 4 and 6, it is clear that thick

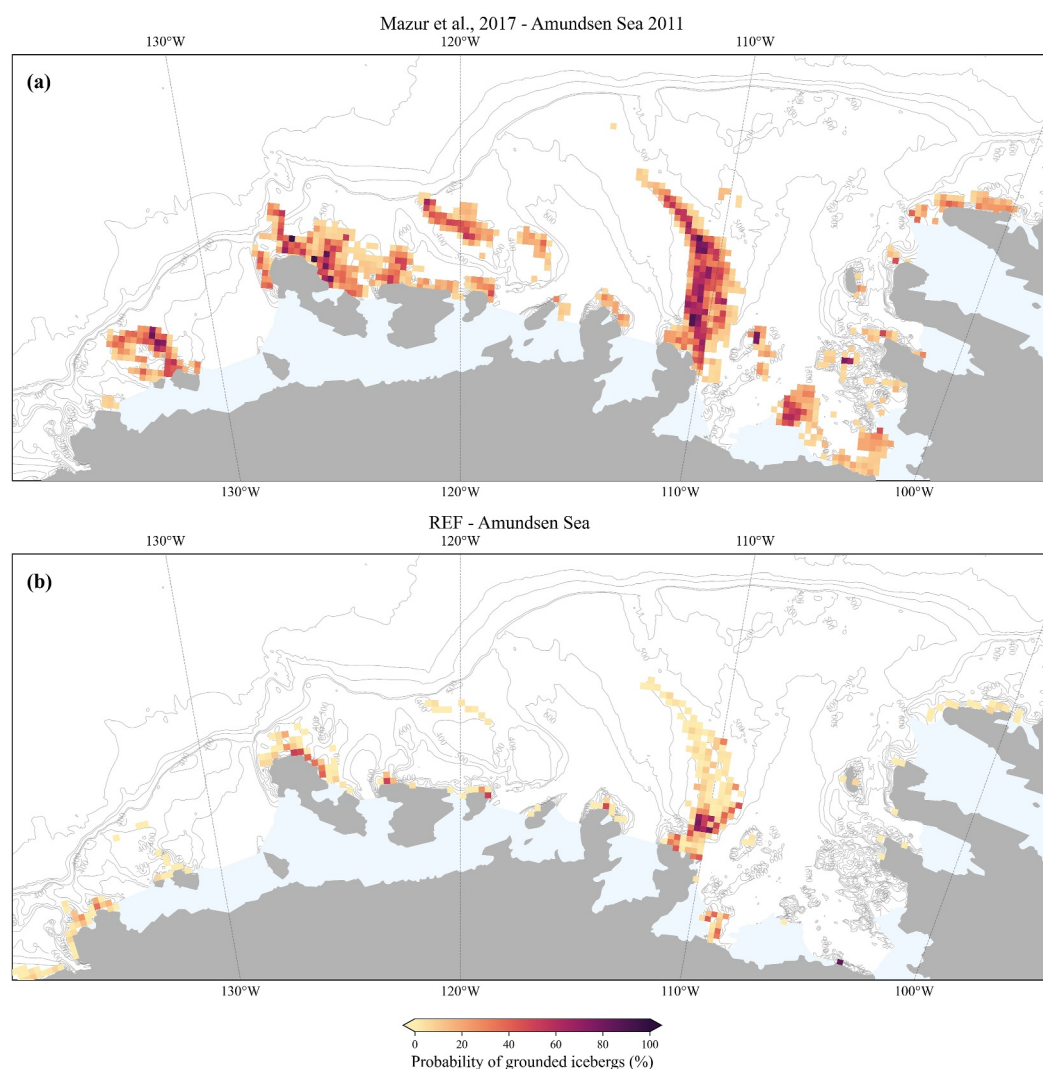


**Figure 5.** Probability of (a) iceberg occurrence from Mazur et al. (2017) inferred from Advanced Synthetic Aperture Radar (ASAR) images with an effective spatial resolution of  $150\text{ m} \times 150\text{ m}$  and (b) grounded icebergs in the REF experiment, in the Amundsen Sea. While iceberg occurrences in Mazur et al. (2017) were calculated for all of 2011, we selected a random single steady-state year in the REF experiment for the comparison, as a repeated-year forcing simulation holds no additional significance. The gray solid lines indicate the bathymetry contours according to the IBCSO database (Arndt et al., 2013), and the light blue shading represents the Antarctic ice shelves. For a clearer comparison, only probabilities higher than 5% in Mazur et al. (2017) are represented.

icebergs melt substantially where they become grounded, resulting in fewer very thick icebergs continuing downstream along ACoC (westward) around the Antarctic coast and then heading north through Iceberg Alley.

Although the Antarctic continental shelf (here defined up to the 1,500 m isobath southward of  $60^\circ\text{S}$ ) represents a small fraction of the Southern Ocean, it receives slightly more than half of the meltwater from all Antarctic icebergs (Figure 7). In particular,  $631\text{ Gt yr}^{-1}$  of iceberg freshwater ends up on the Antarctic continental shelf in the NoGr experiment, mainly from the Ross West and PIG/Thwaites basins (Figure 7), while the Ronne is the dominant basin for freshwater discharge into the deep ocean, with  $53\text{ Gt yr}^{-1}$  out of  $300\text{ Gt yr}^{-1}$ . The freshwater flux over the Antarctic continental shelf increases considerably, up to  $802\text{ Gt yr}^{-1}$ , when we activate grounding in the REF scenario, with the Totten/Moscow basin increasing the most by  $25\text{ Gt yr}^{-1}$  compared with the NoGr experiment (Figure 7).

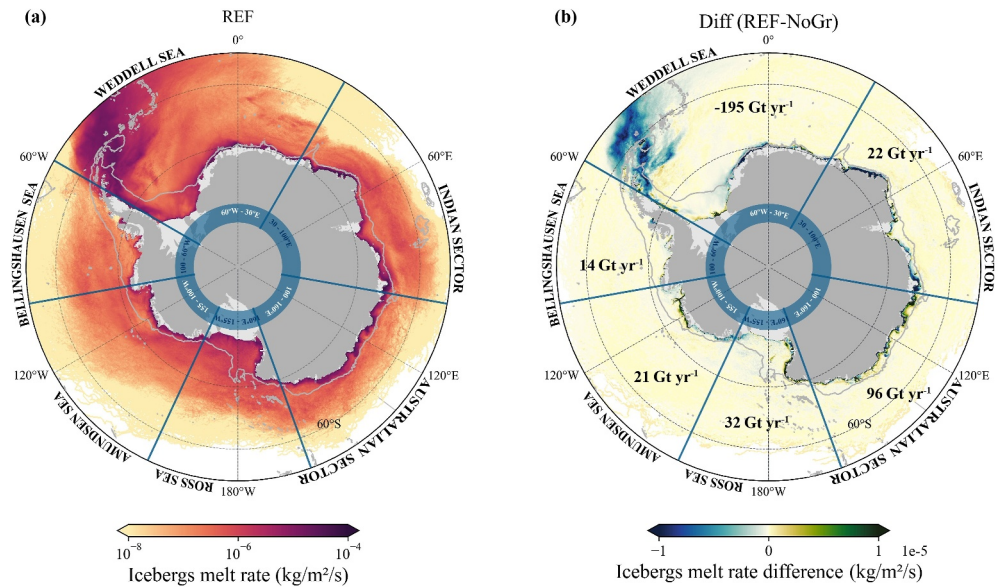


**Figure 6.** Melting distribution per Antarctic sector for (a) REF for 25 years climatology and (b) its difference with the simulation without grounding (REF—NoGr). The melting differences between both experiments correspond to a decrease of  $195 \text{ Gt yr}^{-1}$  in the Weddell Sector and an increase of 22, 96, 32, 21, and  $14 \text{ Gt yr}^{-1}$  for Indian, Australian, the Ross Sea, the Amundsen Sea, and the Bellingshausen Sea sectors, respectively. Blue radial lines indicate the Antarctic sector boundaries, and the 1,500 m isobath corresponding to our definition of the Antarctic continental shelf is represented in gray. The sectors are defined by the following longitudinal boundaries: Weddell Sea ( $60^\circ\text{W}$ – $30^\circ\text{E}$ ), Indian Sector ( $30^\circ\text{E}$ – $100^\circ\text{E}$ ), Australian Sector ( $100^\circ\text{E}$ – $160^\circ\text{E}$ ), Ross Sea ( $160^\circ\text{E}$ – $155^\circ\text{W}$ ), Amundsen Sea ( $155^\circ\text{W}$ – $100^\circ\text{W}$ ), and Bellingshausen Sea ( $100^\circ\text{W}$ – $60^\circ\text{W}$ ). Note that a melt rate of  $10^{-6} \text{ kg m}^{-2} \text{ s}^{-1}$  is equivalent to  $31.5 \text{ mm yr}^{-1}$ ; hence, the total freshwater flux released from icebergs represents the 6.7% of the annual precipitation ( $1.8 \cdot 10^8 \text{ mm yr}^{-1}$ ) in the region.

### 3.3. Impacts on the Sea-Ice Production, Bottom Temperature, and Salinity

Most Antarctic sea ice is produced over the continental shelf (Figure 8c), and the resulting brine-rejection and subsequent deep convection explain the presence of cold and salty water near the sea floor of the southwestern parts of the Ross and Weddell Seas (Figures 8a and 8b). Higher rates of net sea ice production are distributed

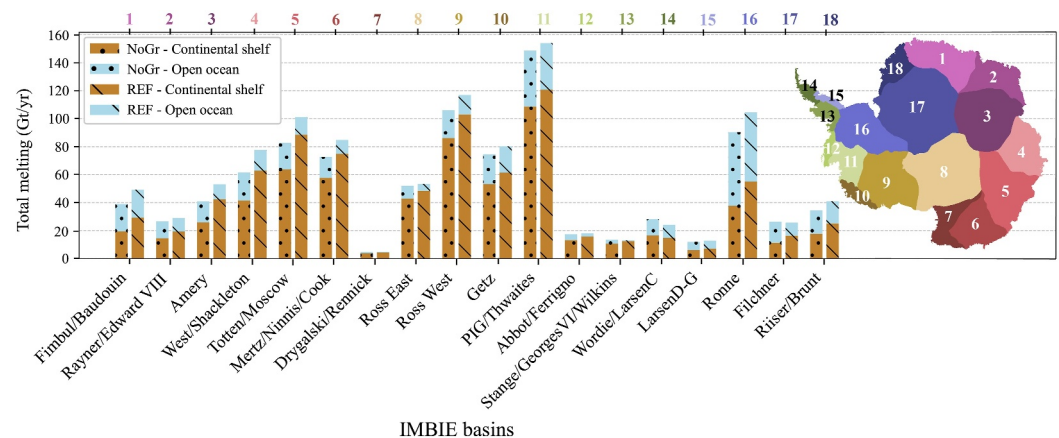


**Figure 7.** Total iceberg melting over the deep ocean (light blue) and the continental shelf (brown) according to the basin from which icebergs were calved, with (REF, hatched) or without (NoGr, dotted) the grounding scheme. To define the different Antarctic basins, we use the basin definitions from the Ice Sheet Mass Balance Inter-comparison Exercise (IMBIE), which comprises 18 ice-sheet drainage basins across Antarctica (Otosaka et al., 2023). The different IMBIE basins are represented and labeled for easier identification. The 1,500 m isobath south of  $60^\circ\text{S}$  is used to define the Antarctic continental shelf, as in Tamsitt et al. (2021) and Morrison et al. (2020). Additionally, the iceberg melting distribution in the domain according to each basin source for the NoGr experiment is represented in Figure S6 in Supporting Information S1.

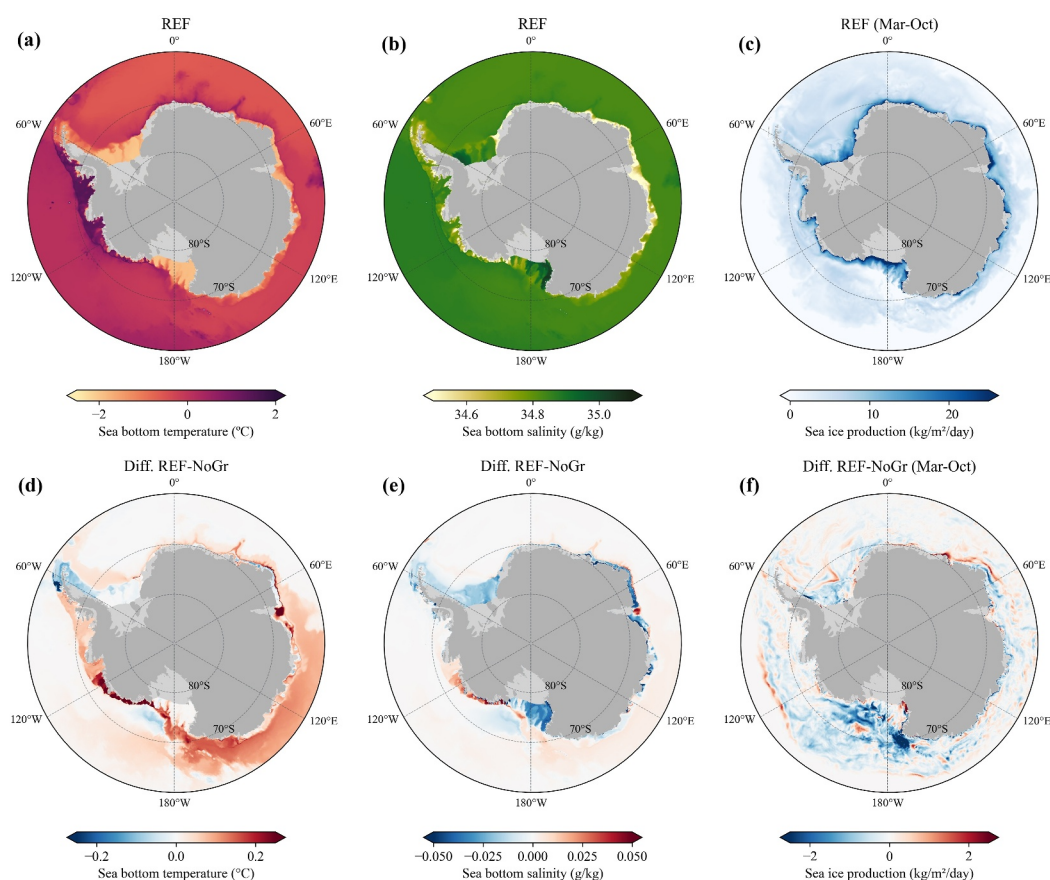


**Figure 8.** (a–c) Sea bottom temperature, salinity and sea-ice production in the REF experiment for the 25 years of climatology and (d–f) the difference with the NoGr experiment for the same period. The 25-year climatology has been calculated only from March to October for sea-ice production, and based on the annual means for temperature and salinity.

relatively homogeneously along the Antarctic coast, with the maximum values simulated in front of the Amery Ice Shelf, specifically over the Mackenzie Bay Polynya, reaching  $129.6 \text{ kg m}^{-2} \text{ day}^{-1}$ . This is not significantly affected by the presence of grounded icebergs in most regions (Figure 8f) because our sea ice model is unaware of the presence of icebergs. Nonetheless, the additional release of freshwater on the continental shelf due to the melting of grounded icebergs can increase the ocean stratification, thereby limiting deep convection. This can be clearly seen in front of Pine Island Glacier (Figure S7 in Supporting Information S1), where the isopycnals and isotherms remain closely spaced and horizontal throughout the period (Figure S7b in Supporting Information S1), whereas in the absence of grounded icebergs (Figure S7a in Supporting Information S1), convection eventually intensifies, resulting in the tilting of isopycnals and the dominance of denser and colder shelf waters (below  $-1.5^\circ\text{C}$ ) throughout the entire water column. The enhanced stratification over the continental shelf also explains the freshening effect of iceberg grounding near the sea floor of the Ross and Weddell Seas (Figure 8e). This freshening is nonetheless not sufficient to produce a regime shift to warm temperatures and high ice-shelf melt rates as described in Mathiot and Jourdain (2023) and Naughten et al. (2021). Indeed, basal melt increases only slightly, with a total of  $3.9 \text{ Gt yr}^{-1}$  (4.6%) beneath the Ross Ice Shelf and of  $3.7 \text{ Gt yr}^{-1}$  (1.4%) beneath the Ronne-Filchner Ice Shelf.

In the western part of the Amundsen Sea, the additional freshwater released mainly by the icebergs grounded on the eastern side of Bear Ridge is responsible for ocean warming at depth that exceeds  $0.2^\circ\text{C}$  (Figure 8d). This warming can be attributed to the topographic influence of Bear Ridge, which delineates distinct oceanographic regimes within the Amundsen Sea by acting as a barrier. Additionally, the surface meltwater is predominantly transported ACoC downstream (westward), primarily enhancing water-column stratification over the continental shelf. This stratification isolates dense deep waters from the colder and fresher surface layers, preventing heat loss

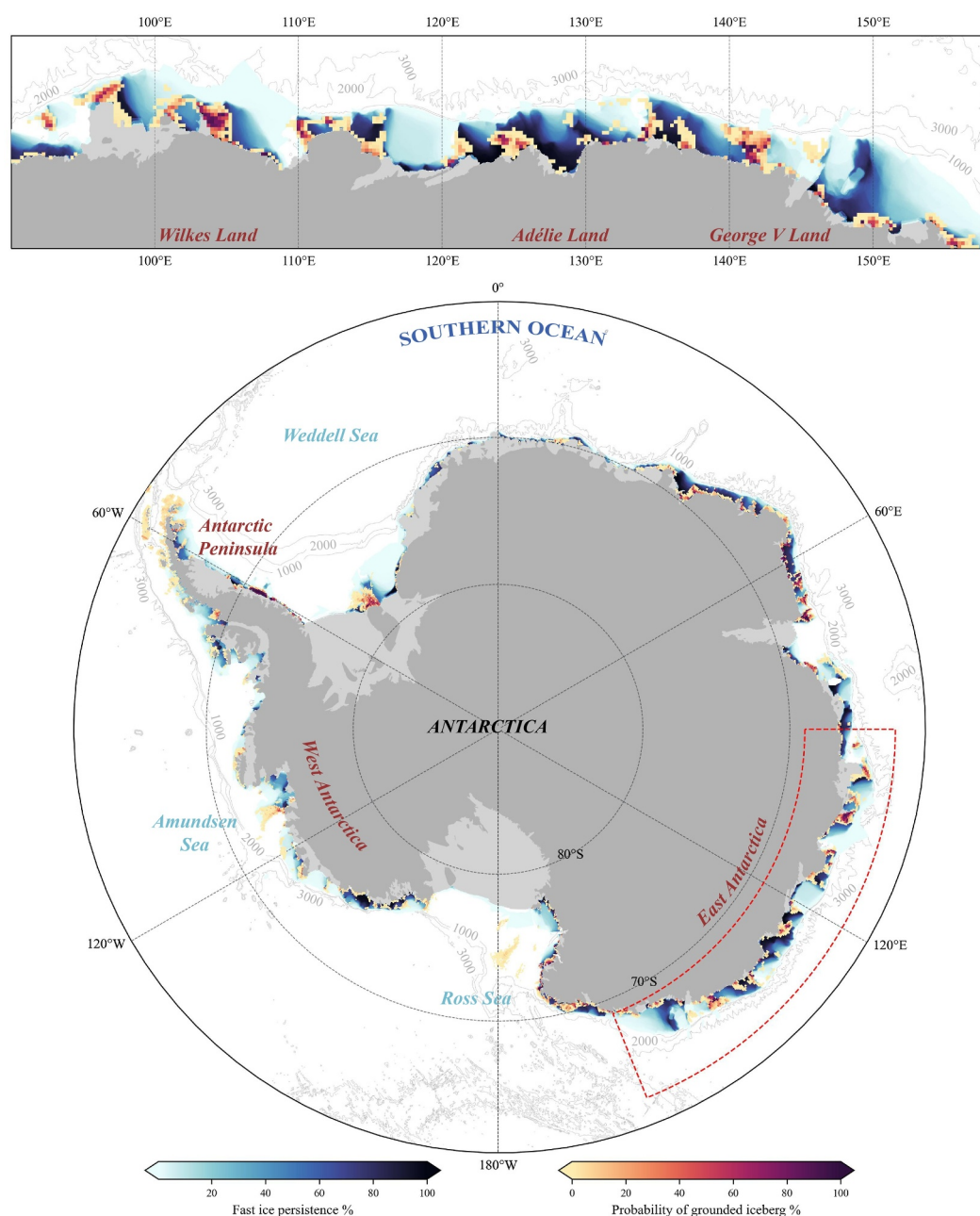


**Figure 9.** Probability of grounded icebergs (25-year climatology of REF experiment) together with the distribution of fast ice persistence calculated from 432 contiguous maps of the NASA Moderate Resolution Imaging Spectroradiometer (Fraser et al., 2021) for the 2000–2018 period and expressed as a percentage of time covering each pixel. The upper panel shows a zoomed-in view of the East Antarctica sector to highlight regional details of fast-ice persistence and grounding probability. Bathymetry contours, from 1,000 to 3,000 m, are represented as solid gray lines.

to the atmosphere and allowing these deep waters to warm and become saltier. Thus, this bottom warming over the Antarctic continental shelf close to the base of the ice shelves promotes the subsequent increase in ice-shelf melting (e.g., from 82 to 91 Gt yr<sup>-1</sup> for Dotson). This could favor more iceberg calving in the western Amundsen Sea and, consequently, higher melt rates, that is, a positive feedback (as already appreciated in Bett et al., 2020; Walker et al., 2007). However, it is important to be aware that this ocean's response may not be entirely realistic, as the sea ice–iceberg interaction is absent, allowing sea ice to pass straight through grounded bergs and thereby

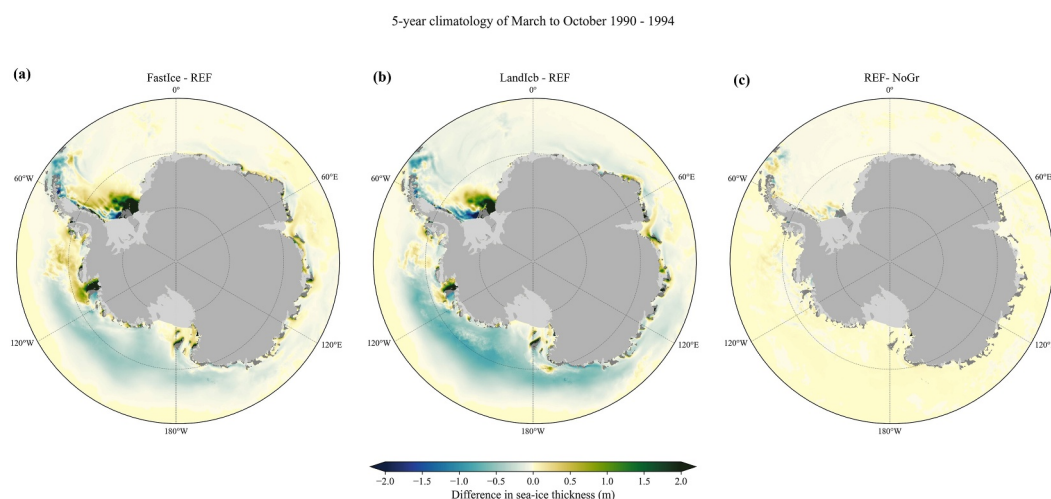


**Figure 10.** Differences in sea-ice thickness from March to October over the 5-year climatology (after a 10-year spin up) due to grounding icebergs and simple iceberg–sea-ice interactions are shown in (a) FastIce minus REF and (b) LandIcb minus REF, and when the sea ice dynamics are not influenced by grounded icebergs in (c) REF minus NoGr. The REF grounded iceberg mask derived from the 25-year climatology is represented in dark gray.

preventing the formation of the Amundsen Sea Polynya (see Section 4 for the two simple approaches implemented as a first attempt to simulate these coastal polynyas).

The other location where the melting of grounded icebergs induces substantial near-sea-floor ocean warming is Prydz Bay, in front of the Amery Ice Shelf (Figure 8d). The warm and salty response at depth occurs within the Prydz Bay gyre (Jin et al., 2024) promoting an increase of the Amery Ice Shelf basal melting of  $7.9 \text{ Gt yr}^{-1}$ . As a result, this enhanced melting drives more water out of the cavity along the western ice shelf base, increasing the barotropic ocean circulation locally by up to  $0.2 \text{ Sv}$  (see Figure S8 in Supporting Information S1).

#### 4. Discussion

In this study, we have implemented an oversimplified iceberg grounding scheme that changes the spatial distribution of iceberg meltwater. In the absence of a high temporal and spatial resolution data set of grounded icebergs across the circumpolar region, it is currently not possible to comprehensively evaluate the fidelity of our simulations. Nevertheless, as grounded icebergs are known to promote fast-ice formation, the spatial patterns of fast-ice presence and persistence can offer indirect evidence of likely grounding locations. For this reason, we created a climatological distribution of fast ice persistence based on fast-ice time series derived from 432 NASA Moderate Resolution Imaging Spectroradiometer maps from the 2000–2018 period, provided by Fraser et al. (2021). The climatological persistence distribution was calculated as the percentage of time each grid cell was covered by fast ice. Hence, Figure 9 presents a comparison between the probability of grounded icebergs from the 25-year REF experiment and the climatological fast-ice persistence distribution. It is noteworthy that fast-ice persistence is nearly 100% just eastward of the areas where grounded iceberg occurrence is high in our simulations (Figure 9), which reflects the expected blocking effect of grounding icebergs, as in the Antarctic coastal region sea ice generally drifts westward (downstream) under prevailing easterly winds and westward currents and fronts (Ian, 1989; Krauzig et al., 2024). Hence, grounded icebergs form a downstream barrier for the fast-ice, helping to maintain its extent and providing it stability. This gives us confidence that iceberg grounding occurs at the right locations in our simulations.

Analyzing where iceberg grounding occurs may provide simple ways to represent the effect of grounded icebergs in ocean–sea-ice models that do not represent Lagrangian icebergs. Consistent with Li et al. (2017), we find that 91% of grounding occurrences happen on bathymetry shallower than 400 m, primarily on the eastern side of bathymetric features and especially close to the coast of East Antarctica and in the Antarctic Peninsula sector (Figure 9). The remaining deeper groundings (9%) are found grounded mainly between 400 and 550 m, with the deepest at 552 m. Alternatively, icebergs interact with 31% of the grid cells corresponding to bathymetric features of the Antarctic continental shelf shallower than 400 m. When considering only the grid cells with eastward-

facing slopes, 41% of them cause iceberg grounding at some point. These rules could be used to approximate the distribution of grounded icebergs by applying a simple bathymetric criterion, offering a practical way for ocean–sea-ice models to impose static features and capture, for instance, fast ice and polynya formation without the need for explicit Lagrangian iceberg tracking.

It is important to acknowledge that our method is suitable for identifying possible grounding locations but does not resolve the dynamic iceberg–seafloor interaction or the duration of iceberg grounding events (as seen in Figure 5). One plausible explanation for the generally lower frequency of grounded icebergs in the REF simulation compared to observations is the clustering of small icebergs into fewer individual Lagrangian particles. This approach reduces the probability of at least one small iceberg continuously occupying or replacing another within each grid cell over time. Although their thicknesses are thinner and may be unable to ground, only the smallest class—with areas smaller than  $0.074 \text{ km}^2$  ( $a_k < 1.5, h_{\text{iso}}^2$ )—exhibits a thinner thickness than its ice-shelf source (considering 10 iceberg classes). Another, and the most plausible explanation, is that the existing grounding physics implemented in our model are extremely simplified, potentially leading to premature ungrounding. Specifically, the NEMO model allows icebergs to unground as soon as the driving stresses point away from the topography, whereas in reality, basal friction would act in all directions, resisting motion and maintaining grounding even when the primary stress vectors shift. Some icebergs have been observed to remain grounded for several decades (Barnes et al., 2018; Grosfeld et al., 2001), and simulating the evolution of iceberg grounding in transient climate simulations would require a more physical representation of the iceberg–bathymetry interactions and real grounding and ungrounding capability schemes instead of the simple scheme used here. Recently, Kostov et al. (2025) have improved the representation of bathymetry–iceberg interactions by including acceleration terms related to gravity, solid-body friction, and sediment resistance. These acceleration and deceleration terms take into account the local slope of the topography and the angle at which an iceberg moves relative to the horizontal plane. Once these developments will be implemented in the NEMO iceberg module, they will enable a more accurate representation of iceberg residence time at grounding sites and improve the local estimation of their melt rates as well as the ocean's response to this freshwater input.

Another important caveat of our simulations is that iceberg meltwater is injected into the ocean surface level. Laboratory experiments indicate that this approximation is only valid if the relative speed of the iceberg with the ocean is smaller than the meltwater plume's vertical velocity (FitzMaurice et al., 2017). Oceanic observations near iceberg A68a (much larger than those represented in our Lagrangian model) indicate that significant vertical mixing is associated with freshwater injection at the base of the iceberg, potentially leading to different impacts on the deep ocean properties over the Antarctic continental shelf (Lucas et al., 2025). Moreover, the modeled sea ice dynamics are unaffected by the presence of icebergs, while real grounded icebergs clearly favor the formation of fast ice (Figure 9). As for grounding, more work would be needed to accurately represent the iceberg–sea-ice interactions for simulating thicker fastened sea-ice cover, including the drag between icebergs and sea ice, as well as sea-ice ridging or breaking due to the redistribution of internal stresses. Nonetheless, we have conducted two extra experiments in which we represent part of these interactions in simple ways (Figure 10). The first approach (hereafter *FastIce*) makes use of the iceberg–fast-ice parameterization of Lemieux et al. (2015, 2016), in which sea ice over a grid cell where at least one iceberg has grounded once incorporates an additional basal stress term to the sea-ice momentum equation and add an isotropic tensile strength to account for sea-ice arch formation. The second approach (hereafter *LandIceb*) consists of treating grid cells in which at least one iceberg has grounded as land cells in NEMO.

For both approaches, we obtain similar sea-ice thickness distribution: thicker sea ice accumulates on the eastern side (upstream) of grounded icebergs, while thinner sea ice is found on the western side (downstream) where coastal polynyas are expected (Figures 10a and 10b). Sea ice is thickened by more than two m in front of Thwaites Glacier, the Ronne-Filchner Ice Shelf, the western Ross Sea, and in East Antarctica. In contrast, implementing iceberg grounding without interaction with sea ice does not significantly impact the sea ice thickness, only in the northern part of the Antarctic Peninsula (Figure 10c).

Our simulations with fast ice reveal the development of an extensive polynya appearing downstream of the grounded icebergs in the Ross Sea (not shown), and propagating throughout the entire Ross Gyre toward the Amundsen Sea (Figures 10a and 10b). This makes both simulations unrealistic in terms of ocean properties, even though the formation of fast ice results in a more realistic sea ice distribution. We suggest retuning the ocean–sea-ice model after the implementation of the fast-ice parameterization. In particular, the relatively low maximum sea

ice fraction imposed in the model was introduced to account for unresolved leads and polynyas. The use of the fast-ice parameterization allows such openings in the sea ice cover, and partly makes this parameter obsolete. This makes both simulations still far from correctly reproducing the underlying ocean dynamics, but including fast-ice formation remains more realistic for large-scale sea ice. Hence, the fast-ice scheme also needs to be improved to avoid overestimating land fast-ice extent and to include processes related to sea ice thermodynamics, specifically adapted to Antarctic continental shelf conditions. Also, we suggest that retuning the ocean–sea-ice model would be needed after the implementation of fast ice.

## 5. Conclusion

In this study, we revisit the iceberg thickness distribution in Southern Ocean simulations by imposing that tabular icebergs inherit the thickness of the ice shelf from which they calve. Using realistic ice-shelf thicknesses along the calving front results in icebergs with a broader thickness distribution and keels deeper than 600 m. Thick icebergs are mostly found over the Antarctic continental shelf and are transported counterclockwise by the ACoC, while smaller icebergs show broader dispersion, reaching easily lower latitudes and being rapidly carried eastward by the ACC. In our simulations, these thicker icebergs interact with 31% of the bathymetric features of the Antarctic continental shelf shallower than 400 m, especially in front of the Ronne-Filchner Ice Shelf and Thwaites Glacier. From these simulations, we estimate the probability of iceberg grounding, which fairly reproduces the satellite observations over the shallow ridges of the Amundsen Sea, and is consistent with the observed fast ice distribution. However, our simple grounding methodology remains unable to accurately represent the residence time of grounded icebergs.

Iceberg melting over the Antarctic continental shelf reaches an average of 631 Gt yr<sup>−1</sup> if icebergs do not interact with bathymetry, and of 802 Gt yr<sup>−1</sup> if a simple grounding scheme is used. Pine Island Glacier/Thwaites and Ross West are the basins contributing the most to this change, increasing by 12 Gt yr<sup>−1</sup> and 17 Gt yr<sup>−1</sup> when icebergs interact with bathymetry. Such additional freshwater injected in an area prone to sea ice production has important consequences for the ocean properties around Antarctica. This freshwater enhances the ocean stratification, limiting deep convection and allowing isolated dense deep waters to become warmer and saltier on some parts of the continental shelf. This effect is particularly pronounced in the Amundsen Sea, where the bottom temperatures and salinities increase by more than 0.2°C and 0.02 g kg<sup>−1</sup>, respectively.

More importantly, grounded icebergs also block drifting sea ice and favor the formation of thick sea ice on the side of the berg facing the currents (eastern side) when a fast-ice parameterization is included. Even though further work is needed to fully model complex sea-ice–iceberg and bathymetry–iceberg interactions, the iceberg module in NEMO can already simulate fast ice blocked by icebergs in regions where high sea-ice persistence is observed in satellite products.

The ice discharge across the Antarctic grounding line is expected to increase in the next decades and centuries, while ice shelves are expected to become thinner (Coulon et al., 2024; Paolo et al., 2023; Seroussi et al., 2020). This suggests that newly calved icebergs will no longer be thick enough to ground on some of the deeper banks. At the same time, enhanced iceberg melting over the continental shelf is expected to increase the content of warm CDW that reaches and melts Antarctic ice shelves (Bett et al., 2020). However, the consequences for the Southern Ocean and climate system are difficult to assess without a model simulating iceberg grounding and iceberg–sea-ice interactions. These processes could also affect the primary production along the iceberg trajectories, significantly impacting the ecosystem dynamics and locally affecting carbon sequestration (Laufkötter et al., 2018; Raiswell et al., 2016; Wu & Hou, 2017).

## Appendix A

### A1. An Objective Definition of the Iceberg Classes

Here we propose an objective definition of the calved iceberg size across  $N$  classes, where the iceberg thickness,  $h$ , depends on the local ice-shelf thickness (and hence varying between ice shelves and along the calving front of a given ice shelf), while the iceberg surface area ( $a$ ) for each individual classes is common across all ice shelves.

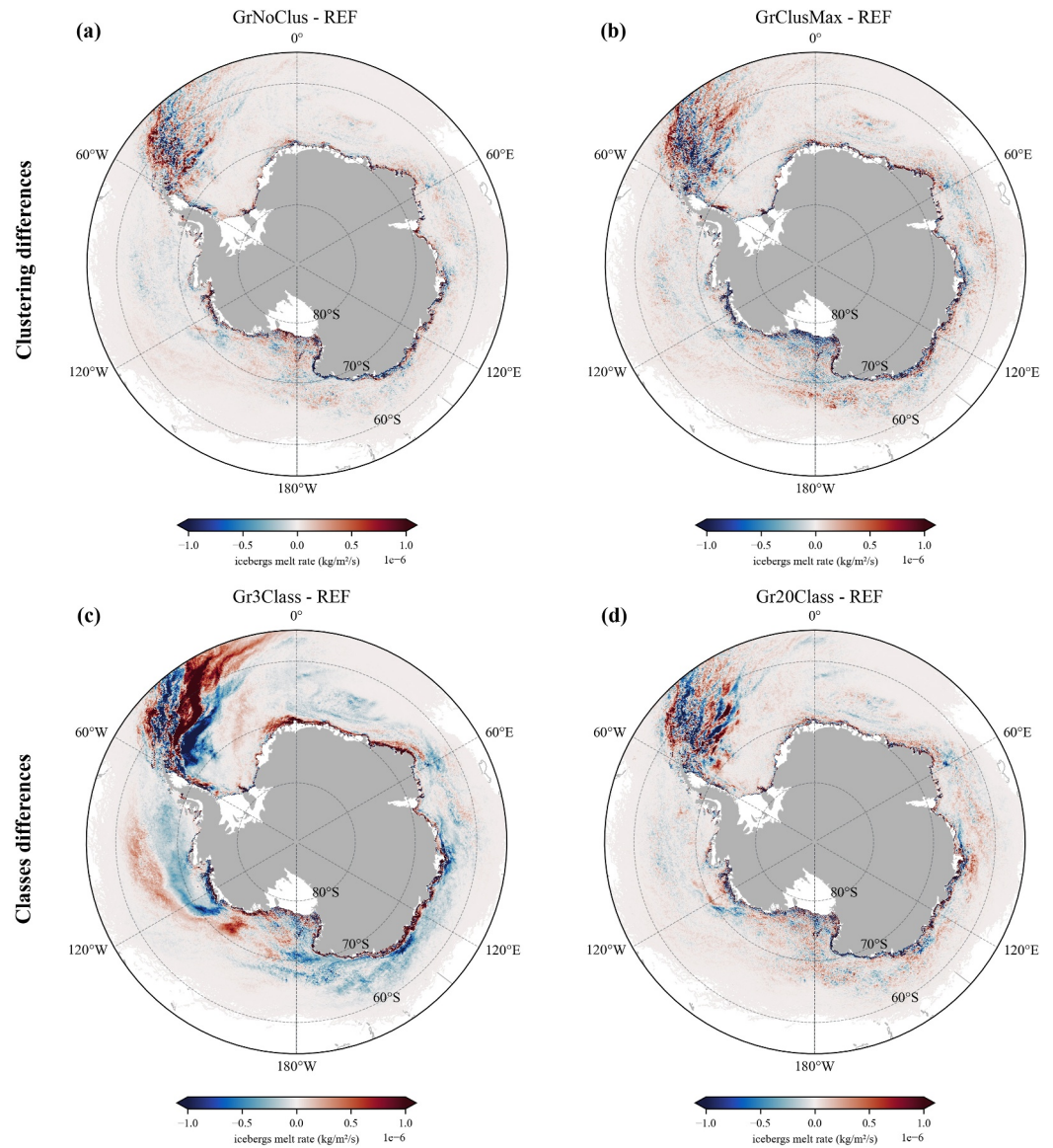


**Figure A1.** Sensitivity of the freshwater distribution to the clustering parameter for (a) No clustering minus clustering with  $R = 2$  (GrNoClus—REF), and (b) Maximum clustering ( $R = 1$ ) minus clustering with  $R = 2$  (GrClusMax—REF), and to the number of iceberg classes for (c) 3 minus 10 classes (Gr3Class—REF) and (d) 20 minus 10 classes (Gr20Class—REF). The comparisons are 25-year averages (after 15 years of spin-up).

For this, the following steps are undertaken: Initially, the iceberg volume distribution is estimated (Equation A4), which implies the definition of the new analytical formulation for iceberg thickness, the probability distribution function of iceberg occurrence, and the calculation of the total iceberg area (from Equations A1 to A3). After integrating the total volume of icebergs and dividing it into  $N$  classes, the area bounds for each class are deduced (Equation A7), as well as the typical surface area and iceberg thickness of each class (Equations A10 and A12). Finally, these values are then used to define the final iceberg width, length, thickness, and mass for each class (Equation A13).

First, we propose a new analytical formulation for iceberg thickness distribution as a function of surface area (Equation A1), using an iceberg length-to-width ratio of 1.5 (see Section 2.2). The largest icebergs are calved with a thickness  $h$  corresponding to the local ice-shelf thickness at the calving front ( $h_{is}$ ). For the classes in which the iceberg width ( $\sqrt{a/1.5}$ ) is smaller than the ice-shelf thickness, the thickness of the calved iceberg is set to the width value:

$$h(a) = \begin{cases} \sqrt{a/1.5} & \text{if } a \leq 1.5 h_{\text{is}}^2 \\ h_{\text{is}} & \text{if } a > 1.5 h_{\text{is}}^2 \end{cases} \quad (\text{A1})$$

According to Tournadre et al. (2016), the probability distribution function of iceberg occurrence as a function of iceberg area in the Southern Ocean is well represented by the following power law that is also consistent with brittle mechanics theory (Åström et al., 2021):

$$f(a) = \mathcal{L}_{\mathcal{T}} a^{-1.5} \quad (\text{A2})$$

where  $\mathcal{L}_{\mathcal{T}}$  is the Tournadre length, a normalization constant with a length dimension (for further details see Appendix D in Tournadre et al. (2016)). If we consider that the iceberg surface area has an upper bound  $a_{\text{max}}$ , either related to the ice-shelf size or imposed as a model parameter, we can estimate the total iceberg area  $A_{\text{tot}}$ :

$$A_{\text{tot}} = \int_0^{a_{\text{max}}} a f(a) da = \mathcal{L}_{\mathcal{T}} \int_0^{a_{\text{max}}} a^{-0.5} da = 2\mathcal{L}_{\mathcal{T}} \sqrt{a_{\text{max}}} \quad (\text{A3})$$

For the sake of implementation simplicity, computational cost, and uniformity of treatment around Antarctica, we choose that icebergs that calve in class  $k$  have the same surface area  $\langle a \rangle_k$  regardless of their calving location around Antarctica. We aim for all classes to represent a similar total ice volume among them. Therefore, we define the iceberg size classes ensuring that the total calved ice mass is equally distributed into them for a typical ice-shelf thickness  $h_{\text{is0}}$  of 222.5 m. We consider this value as the most representative Antarctic ice-shelf thickness at the front, estimated as the calving-front average weighted by the calving flux, ensuring that ice shelves with minimal calving rates do not significantly constrain our selection (Figure S4 in Supporting Information S1). With this typical ice-shelf thickness,  $h_{\text{is0}}$ , the total iceberg area  $A_{\text{tot}}$ ,  $h(a)$  and the probability distribution function of iceberg occurrence per iceberg area in Equation A2, the volume distribution per iceberg surface area,  $g(a) = h a f(a)$ , can be expressed as:

$$g(a) = \begin{cases} \mathcal{L}_{\mathcal{T}}/\sqrt{1.5} & \text{if } a \leq 1.5 h_{\text{is0}}^2 \\ \mathcal{L}_{\mathcal{T}} h_{\text{is0}} a^{-0.5} & \text{if } a > 1.5 h_{\text{is0}}^2 \end{cases} \quad (\text{A4})$$

From Equation A4, the integrated total volume of icebergs in the Southern Ocean that would calve is:

$$V_{\text{tot}} = \int_0^{a_{\text{max}}} g(a) da = \mathcal{L}_{\mathcal{T}} h_{\text{is0}} \left( 2\sqrt{a_{\text{max}}} - \sqrt{1.5} h_{\text{is0}} \right) \quad (\text{A5})$$

Then, we impose that the total iceberg volume in each class is equal to  $V_{\text{tot}}/N$ , where  $N$  is the number of iceberg classes. We then denote  $(a_{k-1}, a_k)$  the area bounds of class  $k$ , with  $k \in [0, N]$ , and we define  $N_{\text{s0}}$ , the number of classes for which  $a_k < 1.5 h_{\text{is0}}^2$  (which can be zero). This yields:

$$\frac{V_{\text{tot}}}{N} = \int_{a_{k-1}}^{a_k} g(a) da = \begin{cases} \frac{\mathcal{L}_{\mathcal{T}}}{\sqrt{1.5}} (a_k - a_{k-1}) & \text{for } 1 \leq k \leq N_{\text{s0}} \\ \mathcal{L}_{\mathcal{T}} \left( 2h_{\text{is0}}\sqrt{a_k} - \sqrt{1.5} h_{\text{is0}}^2 - \frac{a_{k-1}}{\sqrt{1.5}} \right) & \text{for } k = N_{\text{s0}} + 1 \\ 2\mathcal{L}_{\mathcal{T}} h_{\text{is0}} \left( \sqrt{a_k} - \sqrt{a_{k-1}} \right) & \text{for } k > N_{\text{s0}} + 1 \end{cases} \quad (\text{A6})$$

From the previous equation and Equation A5, the area bounds for each individual class are derived. The equations for  $a_k$  are expressed iteratively, as their specific form depends on the total number of iceberg classes,  $N$ , and consequently, on the value of  $N_{s0}$ :

$$\begin{cases} a_0 = 0 \\ a_k = a_{k-1} + \frac{\sqrt{1.5}}{N} h_{is0} (2\sqrt{a_{\max}} - \sqrt{1.5} h_{is0}) & \text{for } k = 1, \dots, N_{s0} \\ a_k = \left( \frac{\sqrt{a_{\max}}}{N} + \frac{\sqrt{1.5}}{2} h_{is0} \left( 1 - \frac{1}{N} \right) + \frac{a_{k-1}}{2\sqrt{1.5} h_{is0}} \right)^2 & \text{for } k = N_{s0} + 1 \\ a_k = \left( \frac{2\sqrt{a_{\max}} - \sqrt{1.5} h_{is0}}{2N} + \sqrt{a_{k-1}} \right)^2 & \text{for } k = N_{s0} + 2, \dots, N \end{cases} \quad (\text{A7})$$

in which it can be verified that  $a_N = a_{\max}$ . During this iteration, we save the number of small icebergs  $N_{s0}$  that verify the second expression of  $a_k$  in Equation A7:

$$N_{s0} = k - 1 \quad \text{if} \quad a_{k-1} < 1.5 h_{is0}^2 \leq a_k \quad (\text{A8})$$

From Equations A7 and A8, we can estimate the typical iceberg surface area,  $\langle a \rangle_k$ , in each class:

$$\langle a \rangle_k = \int_{a_{k-1}}^{a_k} a g(a) da \quad (\text{A9})$$

which is calculated as:

$$\langle a \rangle_k = \begin{cases} \frac{a_{k-1} + a_k}{2} & \text{for } k = 1, \dots, N_{s0} \\ \frac{\frac{h_{is0}^3}{\sqrt{1.5}} a_k^{\frac{3}{2}} - \frac{a_{k-1}^2}{2} - \frac{1.5}{4} h_{is0}^4}{2\sqrt{1.5} h_{is0} \sqrt{a_k} - a_{k-1} - 1.5 h_{is0}^2} & \text{for } k = N_{s0} + 1 \\ \frac{1}{3} \frac{a_k^{\frac{3}{2}} - a_{k-1}^{\frac{3}{2}}}{\sqrt{a_k} - \sqrt{a_{k-1}}} & \text{for } k = N_{s0} + 2, \dots, N \end{cases} \quad (\text{A10})$$

Similarly, we can calculate the typical iceberg height in individual classes, keeping the  $(a_{k-1}, a_k)$  expressions of Equation A7 based on  $h_{is0}$ , but using the actual ice-shelf thickness  $h_{is}$  in Equation A1. Note that  $h_{is}$  will change in each calving grid cell using the full distribution of the ice-shelf thicknesses. To do so, we need to calculate iteratively the number of small icebergs  $N_s$ , as Equation A8 but using now  $h_{is}$ , that verify the first expression of  $a_k$  in Equation A7:

$$N_s = k - 1 \quad \text{if} \quad a_{k-1} < 1.5 h_{is}^2 \leq a_k \quad (\text{A11})$$

$$\langle h \rangle_k = \begin{cases} \frac{1}{(1.5)^{\frac{3}{2}}} \frac{a_k^{\frac{3}{2}} - a_{k-1}^{\frac{3}{2}}}{a_k - a_{k-1}} & \text{for } k = 1, \dots, N_s \\ \frac{2h_{is}^2 \sqrt{a_k} - \frac{a_{k-1}^{\frac{3}{2}}}{(1.5)^2} - \frac{2}{\sqrt{1.5}} h_{is}^3}{2h_{is} \sqrt{a_k} - \frac{a_{k-1}}{\sqrt{1.5}} - \sqrt{1.5} h_{is}^2} & \text{for } k = N_s + 1 \\ h_{is} & \text{for } k = N_s + 2, \dots, N \end{cases} \quad (\text{A12})$$

The final iceberg width, length, thickness and mass of iceberg class  $k$  are:

$$\begin{cases} w_k = \sqrt{\frac{\langle a \rangle_k}{1.5}} \\ \ell_k = \sqrt{1.5 \langle a \rangle_k} \\ h_k = \langle h \rangle_k \\ m_k = \rho_{ice} \langle h \rangle_k \langle a \rangle_k \end{cases} \quad (\text{A13})$$

For less than 14 classes with our parameter values, the first line of Equation A10 is not valid, and  $\langle a \rangle_1$  is calculated from the second line. Figure S9 in Supporting Information S1 illustrates the area bounds, mean surface area, and thickness of icebergs for 3, 10, and 20 classes.

Finally, each class represents the same total volume of icebergs, but there are more icebergs in the smaller size classes. The more frequent calving of small icebergs is realistic and should be accounted for, but the computational cost motivates the use of clusters for the smallest iceberg categories. A Lagrangian particle of class  $k$  is then representative of a cluster of  $n_k$  icebergs of identical characteristics ( $\langle a \rangle_k$ ,  $\langle h \rangle_k$ ). To keep some differences in calving frequencies between classes while limiting the computational cost, we define a clustering parameter,  $R$ , in a way that an iceberg class is not able to produce a Lagrangian particle more than  $R$  times more often than the largest class, which gives:

$$n_k = \max \left\{ 1, \left\lfloor \frac{\langle a \rangle_N \langle h \rangle_N}{R \langle a \rangle_k \langle h \rangle_k} \right\rfloor \right\} \quad (\text{A14})$$

with  $R \geq 1$ .

## A2. Sensitivity Studies of the Freshwater Distribution and Computational Cost to the Number of Classes and Clustering

Iceberg calving produces icebergs of different sizes, from small bergs to giant tabular icebergs (Åström et al., 2021), and while the latter—making up over 95% of the ice volume—are a dominant source of freshwater discharge into the Southern Ocean (England et al., 2020), they only account for less than 4% of the total number of Antarctic icebergs. Consequently, the size distribution of these released icebergs influences the transport of freshwater, and changes in this distribution will impact the magnitude and spatial extent of freshwater contributions from the ice shelves to the open ocean (Enderlin et al., 2016; Rezvanbehbahani et al., 2020; Stern et al., 2016).

According to our 25-year climatological experiments, the iceberg's melting rates are more sensitive to the number of iceberg classes than to the clustering parameter (Figure A1). Although the distribution is smoother across the

**Table A1**

*Description of the NEMO Experiments Used in the Sensitivity Studies and Their Computational Time Efficiency per Year of Simulation (hh:mm) Using 640 CPUs and Excluding a 15-Year Spin-Up Period*

Experiment name	Number of classes	$R$ parameter (clustering)	Computing time range	Computing time median
NoGr	10	2	02:38–03:15	02:46
REF	10	2	02:50–03:20	03:00
GrClusMax	10	1	02:44–03:10	02:45
GrNoClus	10	$\infty$	03:08–04:33	04:00
Gr3Class	3	2	02:51–03:40	02:58
Gr20Class	20	2	02:41–03:15	02:53

*Note.* The clustering parameter,  $R$ , is equal to 1 corresponding to maximum clustering, while  $\infty$  implies no clustering (Figure 3). All experiments except NoGr set all horizontal velocity components to zero as grounding scheme.

Southern Ocean with only subtle variations along the Antarctic coast and iceberg alley, notable differences in the freshwater contribution appear when a lower number of classes is chosen (Figure A1c). In particular, between 10 and 20 classes, the iceberg melting rates persist quite equally, but with fewer classes, the freshwater flux is released further north into the ocean, especially in the Pacific and Atlantic sectors. This can be attributed to the fact that, with only a few classes, most icebergs have the highest thicknesses similar to or the same as their ice shelf source. Consequently, they can be carried by deeper currents, which may transport them further offshore. Similarly, there is slightly more freshwater released close to the Antarctic coast, coinciding with the counter-clockwise path often followed by thicker icebergs, as already appreciated in Figure 4.

The clustering parameter significantly affects the computational cost (Table A1). Using no clustering ( $R \rightarrow \infty$ ) increases the median computational cost by 33%, while using the maximum clustering ( $R = 1$ ) decreases the median computational cost by 8% (with respect to REF). If the experiments are extended to 100 years, the number of particles increase and using the maximum clustering becomes more interesting, with a computing time decreased by  $\sim 20\%$  (Figure A2). The evolution of the number of particle and computing time in the NoGr

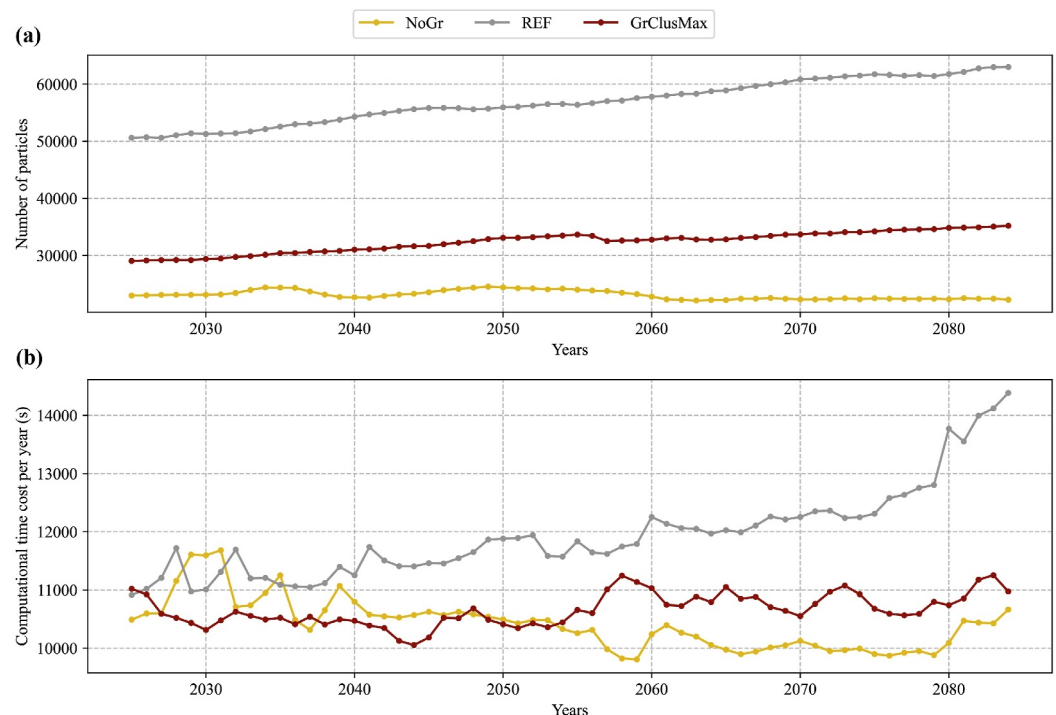


**Figure A2.** Evolution of (a) the number of particles and (b) the computational time per year of simulation in the NoGr, REF and GrClusMax experiments extended to 100 years.

experiment (Table A1, Figure A2) indicates that this long-term drift is due to our grounding scheme: many grounded icebergs remain in the domain for very long periods, which leads to an increase in the number of particles over time and significantly raises the computational cost per year; on the contrary, without grounding, icebergs leave the domain or melt completely relatively fast in the ACC.

### A3. Accumulated Iceberg Volume but Unchanged Melting Rates: Effects on the Water Column

The total mean ice volumes from tabular icebergs found in the Southern Ocean for the 25-year climatology experiments are 5,483, 4,512, and 8,217 Gt for the OLD, NoGr, and REF, respectively. In REF, the amount of volume accumulated is twice the rest of the experiments, consistent with previous findings and confirming that the ice from grounded thick icebergs is progressively accumulated for longer periods. Indeed, extending up to 100 years, the simulations reveal that the total ice volume for the REF experiment keeps growing, drifting from the rest of the time series since the beginning, even from the spin-up period (Figure S10 in Supporting Information S1). In fact, the steady state of ice volume and melting is reached sooner (after 7–9 years) in experiments that do not consider grounding, particularly in the NoGr experiment. Instead, the REF experiment requires at least 15 years of spin-up period to achieve similar melting rates of around  $1,200 \text{ Gt yr}^{-1}$ , maintaining after this period a steady melting rate equal to the rest of the experiments.

As seen before, the ice volume and melting rates are not distributed homogeneously, almost all the total ice volume accumulated in the Southern Ocean — about 483, 391, and 781 Gt for OLD, NoGr and REF, respectively — can be found on the continental shelf (above the 1,000 m isobath) increasing up to 95% when the icebergs ground (between 86.5 and 88.1% when not).

One explanation for why melting does not intensify over time (Figure 11b), despite more icebergs drifting in the Southern Ocean, could be the general cooling of the Antarctic continental shelf, which prevents melting. To better understand the time evolution of the ocean conditions, Figure S11 in Supporting Information S1 shows the mean potential temperature and salinity in those grid cells where icebergs ground at least a quarter of the year (berg grounding frequency  $>0.25$  as in Figure 5) and the same cells for NoGr experiment. Through the Hovmöller diagrams, we observe the potential temperature and salinity of the water column remain stable and stratified for the REF scenario, although without iceberg grounding, the diagram captures colder and saltier conditions for 2030–2065 period at the bottom below 250 m depth. After this period and up to 2084, the conditions in the water column appear to be restabilized.

The removal of iceberg melting is significant, resulting in cold waters dominating the bottom of the water column from 2030 to 2065, reducing the heat budget during this period. Simultaneously, an increase in convection leads to colder temperatures at depth. Consequently, the combined effect of the absence of both iceberg meltwater and grounded icebergs results in even greater dominance of winter cold waters throughout the water column, in line with the observations of Bett et al. (2020). These results demonstrate that iceberg melt is required to mitigate the deep convection in the water column.

### Conflict of Interest

The authors declare no conflicts of interest relevant to this study.

### Data Availability Statement

All data sets used for validation and comparison in this study are open-access. The fast-ice extent data set is provided by Fraser et al. (2021) and can be accessed via <https://doi.org/10.26179/5d267d1ceb60c>. The data set on iceberg occurrence in the Amundsen Sea during 2011, including probability distributions, from Mazur et al. (2017) can be found at <https://doi.pangaea.de/10.1594/PANGAEA.856847>. Additionally, georeferenced Sentinel-1 SAR imagery from 2014 to 2015, with a spatial resolution of 50 m over the Amundsen Sea, is available through Google Earth Engine at [https://developers.google.com/earth-engine/datasets/catalog/COPERNICUS\\_S1\\_GRD](https://developers.google.com/earth-engine/datasets/catalog/COPERNICUS_S1_GRD) (Gorelick et al., 2017). The data set containing the 25-year climatological annual and monthly outputs for the REF simulation of iceberg meltwater flux, and mean and maximum iceberg thickness —for the entire Southern Ocean south of  $52.25^\circ\text{S}$ , normalized and per basin— as well as the grounded icebergs masks, is published in open access in Zenodo under the following <https://doi.org/10.5281/zenodo.15747365>. Additionally, the normalized 30-year climatology of iceberg melt per IMBIE basin from the NoGr experiment is available on

Zenodo under the following <https://doi.org/10.5281/zenodo.14020895>. The revised code for the NEMO iceberg module will be uploaded and documented, and will be publicly available at the GitLab repository: <https://forge.nemo-ocean.eu/>.

### Acknowledgments

This research was supported by Ocean Cryosphere Exchanges in Antarctica: Impacts on Climate and the Earth system, OCEAN ICE, which is funded by the European Union, Horizon Europe Funding Programme for research and innovation under Grant 101060452, 10.3030/101060452. OCEAN ICE contribution number 24. This work was funded by UK Research and Innovation (UKRI) under the UK government's Horizon Europe funding Guarantee, Grant 10048443. This study has received funding from Agence Nationale de la Recherche—France 2030 as part of the PEPR TRACCS programme under Grant ANR-22-EXTR-0008 (IMPRESSION-ESM) and ANR-22-EXTR-0010 (ISCLim). This work was granted access to the high-performance computing (HPC) resources of TGCC under allocation A0140106035 and A160106035 attributed by GENCI. The authors are very grateful to the editor, Dr. Anna Wählin, and to the two reviewers, Dr. Juliana Marson and Dr. Robert Marsh, for their many useful comments and suggestions. The authors are also grateful to Dr. Aleksandra Mazur for sharing her iceberg occurrence data set.

### References

- Ackermann, L., Rackow, T., Himstedt, K., Gierz, P., Knorr, G., & Lohmann, G. (2024). A comprehensive Earth system model (AWI-ESM2. 1) with interactive icebergs: Effects on surface and deep-ocean characteristics. *Geoscientific Model Development*, 17(8), 3279–3301. <https://doi.org/10.5194/gmd-17-3279-2024>
- Arndt, J. E., Schenke, H. W., Jakobsson, M., Nitsche, F. O., Buys, G., Goleby, B., et al. (2013). The international bathymetric chart of the Southern Ocean (IBCSO) Version 1.0—A new bathymetric compilation covering circum-Antarctic waters. *Geophysical Research Letters*, 40(12), 3111–3117. <https://doi.org/10.1002/grl.50413>
- Åström, J., Cook, S., Enderlin, E. M., Sutherland, D. A., Mazur, A., & Glasser, N. (2021). Fragmentation theory reveals processes controlling iceberg size distributions. *Journal of Glaciology*, 67(264), 603–612. <https://doi.org/10.1017/jog.2021.14>
- Barnes, D. K., Fleming, A., Sands, C. J., Quartino, M. L., & Derigibis, D. (2018). Icebergs, sea ice, blue carbon and Antarctic climate feedbacks. *Philosophical Transactions of the Royal Society A: Mathematical, Physical and Engineering Sciences*, 376(2122), 20170176. <https://doi.org/10.1098/rsta.2017.0176>
- Beaman, R. J., & Harris, P. T. (2005). Bioregionalization of the George V Shelf, East Antarctica. *Continental Shelf Research*, 25(14), 1657–1691. <https://doi.org/10.1016/j.csr.2005.04.013>
- Benn, D. I., & Åström, J. A. (2018). Calving glaciers and ice shelves. *Advances in Physics X*, 3(1), 1513819. <https://doi.org/10.1080/23746149.2018.1513819>
- Bett, D. T., Holland, P. R., Naveira Garabato, A. C., Jenkins, A., Dutrieux, P., Kimura, S., & Fleming, A. (2020). The impact of the Amundsen Sea freshwater balance on ocean melting of the West Antarctic Ice Sheet. *Journal of Geophysical Research: Oceans*, 125(9), e2020JC016305. <https://doi.org/10.1029/2020jc016305>
- Bigg, G. R., Wadley, M. R., Stevens, D. P., & Johnson, J. A. (1997). Modelling the dynamics and thermodynamics of icebergs. *Cold Regions Science and Technology*, 26(2), 113–135. [https://doi.org/10.1016/S0165-232X\(97\)00012-8](https://doi.org/10.1016/S0165-232X(97)00012-8)
- Bonnet, P., Yastrebov, V. A., Queutey, P., Leroyer, A., Mangeney, A., Castelnau, O., et al. (2020). Modelling capsizing icebergs in the open ocean. *Geophysical Journal International*, 223(2), 1265–1287. <https://doi.org/10.1093/gji/ggaa353>
- Boucher, O., Servonnat, J., Albright, A. L., Aumont, O., Balkanski, Y., Bastrikov, V., et al. (2020). Presentation and evaluation of the IPSL-CM6A-LR climate model. *Journal of Advances in Modeling Earth Systems*, 12(7), e2019MS002010. <https://doi.org/10.1029/2019ms002010>
- Coulon, V., Klose, A. K., Kittel, C., Edwards, T., Turner, F., Winkelmann, R., & Pattyn, F. (2024). Disentangling the drivers of future Antarctic ice loss with a historically calibrated ice-sheet model. *The Cryosphere*, 18(2), 653–681. <https://doi.org/10.5194/tc-18-653-2024>
- Davison, B. J., Hogg, A. E., Gourmelen, N., Jakob, L., Wuite, J., Nagler, T., et al. (2023). Annual mass budget of Antarctic ice shelves from 1997 to 2021. *Science Advances*, 9(41), eadi0186. <https://doi.org/10.1126/sciadv.adi0186>
- Devilliers, M., Swingedouw, D., Mignot, J., Deshayes, J., Garric, G., & Ayache, M. (2021). A realistic Greenland ice sheet and surrounding glaciers and ice caps melting in a coupled climate model. *Climate Dynamics*, 57(9), 2467–2489. <https://doi.org/10.1007/s00382-021-05816-7>
- Dierkes, W. (2013). Sea ice monitoring by synthetic aperture radar. *Oceanography*, 26(2), 100–111. <https://doi.org/10.5670/oceanog.2013.33>
- Dowdeswell, J., & Bamber, J. (2007). Keel depths of modern Antarctic icebergs and implications for sea-floor scouring in the geological record. *Marine Geology*, 243(1–4), 120–131. <https://doi.org/10.1016/j.margeo.2007.04.008>
- Enderlin, E., Hamilton, G. S., Straneo, F., & Sutherland, D. A. (2016). Iceberg meltwater fluxes dominate the freshwater budget in Greenland's iceberg-congested glacial fjords. *Geophysical Research Letters*, 43(21), 11–287. <https://doi.org/10.1002/2016gl070718>
- England, M. R., Wagner, T. J., & Eisenman, I. (2020). Modeling the breakup of tabular icebergs. *Science Advances*, 6(51), eabd1273. <https://doi.org/10.1126/sciadv.abd1273>
- European Space Agency. (2019). Sentinel data access overview. Retrieved from <https://sentinel.esa.int/web/sentinel/sentinel-data-access>
- FitzMaurice, A., Cenedese, C., & Straneo, F. (2017). Nonlinear response of iceberg side melting to ocean currents. *Geophysical Research Letters*, 44(11), 5637–5644. <https://doi.org/10.1002/2017gl073585>
- Fraser, A. D., Massom, R., Handcock, M. S., Reid, P., Ohshima, K. I., Raphael, M. N., et al. (2021). Eighteen-year record of circum-Antarctic landfast-sea-ice distribution allows detailed baseline characterisation and reveals trends and variability. *The Cryosphere*, 15(11), 5061–5077. <https://doi.org/10.5194/tc-15-5061-2021>
- Fricker, H. A., Young, N. W., Allison, I., & Coleman, R. (2002). Iceberg calving from the Amery ice shelf, East Antarctica. *Annals of Glaciology*, 34, 241–246. <https://doi.org/10.3189/172756402781817581>
- Gladstone, R. M., Bigg, G. R., & Nicholls, K. W. (2001). Iceberg trajectory modeling and meltwater injection in the Southern Ocean. *Journal of Geophysical Research*, 106(C9), 19903–19915. <https://doi.org/10.1029/2000jc000347>
- Gorelick, N., Hancher, M., Dixon, M., Ilyushchenko, S., Thau, D., & Moore, R. (2017). Google Earth Engine: Planetary-scale geospatial analysis for everyone. *Remote Sensing of Environment*, 202, 18–27. <https://doi.org/10.1016/j.rse.2017.06.031>
- Griffies, S. M., Biastoch, A., Böning, C., Bryan, F., Danabasoglu, G., Chassignet, E. P., et al. (2009). Coordinated ocean-ice reference experiments (COREs). *Ocean Modelling*, 26(1–2), 1–46. <https://doi.org/10.1016/j.ocemod.2008.08.007>
- Grosfeld, K., Schröder, M., Fahrbach, E., Gerdes, R., & Mackensen, A. (2001). How iceberg calving and grounding change the circulation and hydrography in the Filchner Ice Shelf–Ocean System. *Journal of Geophysical Research*, 106(C5), 9039–9055. <https://doi.org/10.1029/2000jc000601>
- Hou, S., & Shi, J. (2021). Variability and formation mechanism of polynyas in Eastern Prydz Bay, Antarctica. *Remote Sensing*, 13(24), 5089. <https://doi.org/10.3390/rs13245089>
- Huot, P.-V., Fichefet, T., Jourdain, N. C., Mathiot, P., Rousset, C., Kittel, C., & Fettweis, X. (2021). Influence of ocean tides and ice shelves on ocean–ice interactions and dense shelf water formation in the D'Urville Sea, Antarctica. *Ocean Modelling*, 162, 101794. <https://doi.org/10.1016/j.ocemod.2021.101794>
- Ian, A. (1989). Pack-Ice Drift off East Antarctica and some implications. *Annals of Glaciology*, 12, 1–8. <https://doi.org/10.1017/s0260305500006881>
- Jin, J., Payne, A. J., & Bull, C. Y. (2024). Current reversal leads to regime change in Amery Ice Shelf cavity in the twenty-first century. *EGU sphere*, 2024, 1–26.

- Jongma, J. I., Driesschaert, E., Fichet, T., Goosse, H., & Renssen, H. (2009). The effect of dynamic–thermodynamic icebergs on the Southern Ocean climate in a three-dimensional model. *Ocean Modelling*, 26(1–2), 104–113. <https://doi.org/10.1016/j.ocemod.2008.09.007>
- Kobayashi, S., Ota, Y., Harada, Y., Ebata, A., Mori, M., Onoda, H., et al. (2015). The JRA-55 reanalysis: General specifications and basic characteristics. *Journal of the Meteorological Society of Japan Series II*, 93(1), 5–48. <https://doi.org/10.2151/jmsj.2015-001>
- Kostov, Y., Holland, P. R., Hogan, K. A., Smith, J. A., Jourdain, N. C., Mathiot, P., et al. (2025). Modelled dynamics of floating and grounded icebergs, with application to the Amundsen Sea. *EGU sphere*, 2025, 1–46. <https://doi.org/10.5194/egusphere-2025-2423>
- Krauzig, N., Flocco, D., Kern, S., & Zambianchi, E. (2024). Exploring sea ice transport dynamics at the eastern gate of the Ross Sea. *Deep Sea Research Part II: Topical Studies in Oceanography*, 218, 105428. <https://doi.org/10.1016/j.dsr2.2024.105428>
- Kusahara, K., Williams, G. D., Tamura, T., Massom, R., & Hasumi, H. (2017). Dense shelf water spreading from Antarctic coastal polynyas to the deep Southern Ocean: A regional circumpolar model study. *Journal of Geophysical Research: Oceans*, 122(8), 6238–6253. <https://doi.org/10.1002/2017jc012911>
- Large, W. G., & Yeager, S. G. (2004). Diurnal to decadal global forcing for ocean and sea-ice models: The data sets and flux climatologies. *National Center for Atmospheric Research Boulder*.
- Laufkötter, C., Stern, A. A., John, J. G., Stock, C. A., & Dunne, J. P. (2018). Glacial iron sources stimulate the southern ocean carbon cycle. *Geophysical Research Letters*, 45(24), 13–377. <https://doi.org/10.1029/2018gl079797>
- Lemieux, J.-F., Dupont, F., Blain, P., Roy, F., Smith, G. C., & Flato, G. M. (2016). Improving the simulation of landfast ice by combining tensile strength and a parameterization for grounded ridges. *Journal of Geophysical Research: Oceans*, 121(10), 7354–7368. <https://doi.org/10.1002/2016jc012006>
- Lemieux, J.-F., Tremblay, L. B., Dupont, F., Plante, M., Smith, G. C., & Dumont, D. (2015). A basal stress parameterization for modeling landfast ice. *Journal of Geophysical Research: Oceans*, 120(4), 3157–3173. <https://doi.org/10.1002/2014jc010678>
- Li, T., Liu, Y., Cheng, X., Ouyang, L., Li, X., Liu, J., et al. (2017). The effect of seafloor topography in the Southern Ocean on tabular iceberg drifting and grounding. *Science China Earth Sciences*, 60(4), 697–706. <https://doi.org/10.1007/s11430-016-9014-5>
- Lucas, N. S., Brearley, J. A., Hendry, K. R., Spira, T., Braakmann-Folmann, A., Abrahamsen, E. P., et al. (2025). Giant iceberg meltwater increases upper-ocean stratification and vertical mixing. *Nature Geoscience*, 18(4), 1–8. <https://doi.org/10.1038/s41561-025-01659-7>
- MacAyeal, D. R., Scambos, T. A., Hulbe, C. L., & Fahnestock, M. A. (2003). Catastrophic ice-shelf break-up by an ice-shelf-fragment-capsize mechanism. *Journal of Glaciology*, 49(164), 22–36. <https://doi.org/10.3189/172756503781830863>
- MacKie, E. J., Millstein, J., & Serafin, K. A. (2024). 47 years of large Antarctic calving events: Insights from extreme value theory. *Geophysical Research Letters*, 51(23), e2024GL112235. <https://doi.org/10.1029/2024gl112235>
- Madec, G., & the NEMO System Team. (2022). NEMO ocean engine (v4.2). *Zenodo*. (Computer software manual No. 27). <https://doi.org/10.5281/zenodo.6334656>
- Marsh, R., Ivchenko, V., Skliris, N., Alderson, S., Bigg, G. R., Madec, G., et al. (2015). NEMO-ICB (v1.0): Interactive icebergs in the NEMO ocean model globally configured at eddy-permitting resolution. *Geoscientific Model Development*, 8(5), 1547–1562. <https://doi.org/10.5194/gmd-8-1547-2015>
- Martin, T., & Adcroft, A. (2010). Parameterizing the fresh-water flux from land ice to ocean with interactive icebergs in a coupled climate model. *Ocean Modelling*, 34(3–4), 111–124. <https://doi.org/10.1016/j.ocemod.2010.05.001>
- Massom, R. (2003). Recent iceberg calving events in the Ninnis Glacier region, East Antarctica. *Antarctic Science*, 15(2), 303–313. <https://doi.org/10.1017/s0954102003001299>
- Massom, R., Hill, K., Barbraud, C., Adams, N., Ancel, A., Emmerson, L., & Pook, M. J. (2009). Fast ice distribution in Adélie Land, East Antarctica: Interannual variability and implications for emperor penguins *Aptenodytes forsteri*. *Marine Ecology Progress Series*, 374, 243–257. <https://doi.org/10.3354/meps07734>
- Massom, R., Hill, K., Lytle, V., Worby, A., Paget, M., & Allison, I. (2001). Effects of regional fast-ice and iceberg distributions on the behaviour of the Mertz Glacier polynya, East Antarctica. *Annals of Glaciology*, 33, 391–398. <https://doi.org/10.3189/172756401781818518>
- Massom, R., & Stammerjohn, S. E. (2010). Antarctic sea ice change and variability—physical and ecological implications. *Polar Science*, 4(2), 149–186. <https://doi.org/10.1016/j.polar.2010.05.001>
- Mathiot, P., Jenkins, A., Harris, C., & Madec, G. (2017). Explicit representation and parametrised impacts of under ice shelf seas in the z\* coordinate ocean model NEMO 3.6. *Geoscientific Model Development*, 10(7), 2849–2874. <https://doi.org/10.5194/gmd-10-2849-2017>
- Mathiot, P., & Jourdain, N. C. (2023). Southern Ocean warming and Antarctic ice shelf melting in conditions plausible by late 23rd century in a high-end scenario. *Ocean Science*, 19(6), 1595–1615. <https://doi.org/10.5194/os-19-1595-2023>
- Mazur, A., Wählin, A. K., & Krężel, A. (2017). An object-based SAR image iceberg detection algorithm applied to the Amundsen Sea. *Remote Sensing of Environment*, 189, 67–83. <https://doi.org/10.1016/j.rse.2016.11.013>
- Merino, N., Le Sommer, J., Durand, G., Jourdain, N. C., Madec, G., Mathiot, P., & Tournadre, J. (2016). Antarctic icebergs melt over the Southern Ocean: Climatology and impact on sea ice. *Ocean Modelling*, 104, 99–110. <https://doi.org/10.1016/j.ocemod.2016.05.001>
- Morlighem, M. (2022). *MEaSUREs BedMachine Antarctica, Version 3*. NASA National Snow and Ice Data Center Distributed Active Archive Center. <https://doi.org/10.5067/FPSU0V1MWUB6>
- Morlighem, M., Rignot, E., Binder, T., Blankenship, D., Drews, R., Eagles, G., et al. (2020). Deep glacial troughs and stabilizing ridges unveiled beneath the margins of the Antarctic ice sheet. *Nature Geoscience*, 13(2), 132–137. <https://doi.org/10.1038/s41561-019-0510-8>
- Morrison, A., Hogg, A. M., England, M. H., & Spence, P. (2020). Warm Circumpolar Deep Water transport toward Antarctica driven by local dense water export in canyons. *Science Advances*, 6(18), eaav2516. <https://doi.org/10.1126/sciadv.aav2516>
- Nakayama, Y., Timmermann, R., Schröder, M., & Hellmer, H. H. (2014). On the difficulty of modeling Circumpolar Deep Water intrusions onto the Amundsen Sea continental shelf. *Ocean Modelling*, 84, 26–34. <https://doi.org/10.1016/j.ocemod.2014.09.007>
- Naughten, K. A., De Rydt, J., Rosier, S. H., Jenkins, A., Holland, P. R., & Ridley, J. K. (2021). Two-timescale response of a large Antarctic ice shelf to climate change. *Nature Communications*, 12(1), 1991. <https://doi.org/10.1038/s41467-021-22259-0>
- NEMO Sea Ice Working Group. (2019). Sea ice modelling integrated initiative (SI<sup>3</sup>)—The NEMO sea ice engine (Tech. Rep. No. 31). <https://doi.org/10.5281/zenodo.3878122>
- Ohshima, K. I., Fukamachi, Y., Williams, G. D., Nishihashi, S., Roquet, F., Kitade, Y., et al. (2013). Antarctic Bottom Water production by intense sea-ice formation in the Cape Darnley polynya. *Nature Geoscience*, 6(3), 235–240. <https://doi.org/10.1038/ngeo1738>
- Otosaka, I. N., Shepherd, A., Ivins, E. R., Schlegel, N.-J., Amory, C., van den Broeke, M. R., et al. (2023). Mass balance of the Greenland and Antarctic ice sheets from 1992 to 2020. *Earth System Science Data*, 15(4), 1597–1616. <https://doi.org/10.5194/essd-15-1597-2023>
- Paolo, F. S., Gardner, A. S., Greene, C. A., Nilsson, J., Schodlok, M. P., Schlegel, N.-J., & Fricker, H. A. (2023). Widespread slowdown in thinning rates of West Antarctic ice shelves. *The Cryosphere*, 17(8), 3409–3433. <https://doi.org/10.5194/tc-17-3409-2023>

- Rackow, T., Wesche, C., Timmermann, R., Hellmer, H. H., Juricke, S., & Jung, T. (2017). A simulation of small to giant Antarctic iceberg evolution: Differential impact on climatology estimates. *Journal of Geophysical Research: Oceans*, 122(4), 3170–3190. <https://doi.org/10.1002/2016jc012513>
- Raiswell, R., Hawkins, J. R., Benning, L. G., Baker, A. R., Death, R., Albani, S., et al. (2016). Potentially bioavailable iron delivery by iceberg-hosted sediments and atmospheric dust to the polar oceans. *Biogeosciences*, 13(13), 3887–3900. <https://doi.org/10.5194/bg-13-3887-2016>
- Remy, J.-P., Becquevort, S., Haskell, T., & Tison, J.-L. (2008). Impact of the B-15 iceberg “stranding event” on the physical and biological properties of sea ice in McMurdo Sound, Ross Sea, Antarctica. *Antarctic Science*, 20(6), 593–604. <https://doi.org/10.1017/s0954102008001284>
- Rezvanbehbahani, S., Stearns, L. A., Keramati, R., Shankar, S., & van der Veen, C. (2020). Significant contribution of small icebergs to the freshwater budget in Greenland fjords. *Communications Earth & Environment*, 1(1), 31. <https://doi.org/10.1038/s43247-020-00032-3>
- Rignot, E., Jacobs, S., Mouginot, J., & Scheuchl, B. (2013). Ice-shelf melting around Antarctica. *Science*, 341(6143), 266–270. <https://doi.org/10.1126/science.1235798>
- Scambos, T., Haran, T. M., Fahnestock, M., Painter, T., & Bohlander, J. (2007). MODIS-based Mosaic of Antarctica (MOA) data sets: Continent-wide surface morphology and snow grain size. *Remote Sensing of Environment*, 111(2–3), 242–257. <https://doi.org/10.1016/j.rse.2006.12.020>
- Scambos, T., Sergienko, O., Sargent, A., MacAyeal, D., & Fastook, J. (2005). ICESat profiles of tabular iceberg margins and iceberg breakup at low latitudes. *Geophysical Research Letters*, 32(23). <https://doi.org/10.1029/2005gl023802>
- Schlosser, F., Friedrich, T., Timmermann, A., DeConto, R. M., & Pollard, D. (2019). Antarctic iceberg impacts on future Southern Hemisphere climate. *Nature Climate Change*, 9(9), 672–677. <https://doi.org/10.1038/s41558-019-0546-1>
- Seroussi, H., Nowicki, S., Payne, A. J., Goelzer, H., Lipscomb, W. H., Abe Ouchi, A., et al. (2020). ISMIP6 Antarctica: A multi-model ensemble of the Antarctic ice sheet evolution over the 21st century. *The Cryosphere Discussions*, 2020(9), 1–54. <https://doi.org/10.5194/tc-14-3033-2020>
- Silva, T., Bigg, G., & Nicholls, K. (2006). Contribution of giant icebergs to the Southern Ocean freshwater flux. *Journal of Geophysical Research*, 111(C3). <https://doi.org/10.1029/2004jc002843>
- Smith, R. S., Mathiot, P., Siahann, A., Lee, V., Cornford, S. L., Gregory, J. M., et al. (2021). Coupling the UK Earth System Model to dynamic models of the Greenland and Antarctic ice sheets. *Journal of Advances in Modeling Earth Systems*, 13(10), e2021MS002520. <https://doi.org/10.1029/2021ms002520>
- Stern, A., Adcroft, A., & Sergienko, O. (2016). The effects of Antarctic iceberg calving-size distribution in a global climate model. *Journal of Geophysical Research: Oceans*, 121(8), 5773–5788. <https://doi.org/10.1002/2016jc011835>
- Stern, A., Johnson, E., Holland, D. M., Wagner, T. J., Wadhams, P., Bates, R., et al. (2015). Wind-driven upwelling around grounded tabular icebergs. *Journal of Geophysical Research: Oceans*, 120(8), 5820–5835. <https://doi.org/10.1002/2015jc010805>
- Stewart, K., Kim, W., Urakawa, S., Hogg, A. M., Yeager, S., Tsujino, H., et al. (2020). JRA55-do-based repeat year forcing datasets for driving ocean–sea-ice models. *Ocean Modelling*, 147, 101557. <https://doi.org/10.1016/j.ocemod.2019.101557>
- Tamsitt, V., England, M. H., Rintoul, S. R., & Morrison, A. (2021). Residence time and transformation of warm Circumpolar Deep Water on the Antarctic continental shelf. *Geophysical Research Letters*, 48(20), e2021GL096092. <https://doi.org/10.1029/2021gl096092>
- Thomas, M., Ridley, J. K., Smith, I. J., Stevens, D. P., Holland, P. R., & Mackie, S. (2023). Future response of Antarctic Continental Shelf temperatures to ice shelf basal melting and calving. *Geophysical Research Letters*, 50(18), e2022GL102101. <https://doi.org/10.1029/2022gl102101>
- Tournadre, J., Bouhier, N., Girard-Ardhuin, F., & Rémy, F. (2015). Large icebergs characteristics from altimeter waveforms analysis. *Journal of Geophysical Research: Oceans*, 120(3), 1954–1974. <https://doi.org/10.1002/2014jc010502>
- Tournadre, J., Bouhier, N., Girard-Ardhuin, F., & Rémy, F. (2016). Antarctic icebergs distributions 1992–2014. *Journal of Geophysical Research: Oceans*, 121(1), 327–349. <https://doi.org/10.1002/2015jc011178>
- Tsujino, H., Urakawa, S., Nakano, H., Small, R. J., Kim, W. M., Yeager, S. G., et al. (2018). JRA-55 based surface dataset for driving ocean–sea-ice models (JRA55-do). *Ocean Modelling*, 130, 79–139. <https://doi.org/10.1016/j.ocemod.2018.07.002>
- Van Achter, G., Fichefet, T., Goosse, H., Pelletier, C., Sterlin, J., Huot, P.-V., et al. (2022). Modelling landfast sea ice and its influence on ocean–ice interactions in the area of the Totten Glacier, East Antarctica. *Ocean Modelling*, 169, 101920. <https://doi.org/10.1016/j.ocemod.2021.101920>
- Van Achter, G., Fichefet, T., Goosse, H., & Moreno-Chamarro, E. (2022). Influence of fast ice on future ice shelf melting in the Totten Glacier area, East Antarctica. *The Cryosphere*, 16(11), 4745–4761. <https://doi.org/10.5194/tc-16-4745-2022>
- Voldoire, A., Saint-Martin, D., Sénési, S., Decharme, B., Alias, A., Chevallier, M., et al. (2019). Evaluation of CMIP6 deck experiments with CNRM-CM6-1. *Journal of Advances in Modeling Earth Systems*, 11(7), 2177–2213. <https://doi.org/10.1029/2019ms001683>
- Wagner, T. J., Dell, R. W., & Eisenman, I. (2017). An analytical model of iceberg drift. *Journal of Physical Oceanography*, 47(7), 1605–1616. <https://doi.org/10.1175/jpo-d-16-0262.1>
- Walker, D. P., Brandon, M. A., Jenkins, A., Allen, J. T., Dowdeswell, J. A., & Evans, J. (2007). Oceanic heat transport onto the Amundsen Sea shelf through a submarine glacial trough. *Geophysical Research Letters*, 34(2). <https://doi.org/10.1029/2006gl028154>
- Wu, S.-Y., & Hou, S. (2017). Impact of icebergs on net primary productivity in the Southern Ocean. *The Cryosphere*, 11(2), 707–722. <https://doi.org/10.5194/tc-11-707-2017>